**Title**

Low-Cost and Scalable Material Designs and Processes for Next-Generation Lithium-Ion Battery Anodes

**Author**

Baucom, Jesse Adam

**Publication Date**

2020

UNIVERSITY OF CALIFORNIA

Los Angeles

# Low-Cost and Scalable Material Designs and Processes for Next-Generation Lithium-Ion Battery Anodes

A dissertation submitted in partial satisfaction of the
requirements for the degree Doctor in Philosophy
in Chemical Engineering

by

Jesse Adam Baucom

2020

# ABSTRACT OF THE DISSERTATION

# Low-Cost and Scalable Material Designs and Processes for Next-Generation Lithium-Ion Batteries

by

Jesse Adam Baucom

Doctor of Philosophy in Chemical Engineering

University of California, Los Angeles, 2020

Professor Yunfeng Lu, Chair

Modern human civilization depends on the production and utilization of vast quantities of energy. While innovations in technology are generally met with applause, discoveries over the potential catastrophic impacts of our current ways of generating energy on our climate and society have prompted worldwide efforts to mitigate these issues. Although environmentally-friendly and sustainable methods for electricity generation such as solar photovoltaic energy hold promise for solving our energy issues, a complete shift towards renewable energy would require the development of grid-scale energy storage systems due to the intermittent nature of such technology. In addition, the automotive industry is undergoing a complete transformation to electrification in

efforts to reduce the environmental impact of vehicles and comply with increasingly stringent regulations, representing yet another urgent need for high-performance energy storage systems.

Of all energy storage technologies for potentially enabling grid storage and electric vehicles, lithium-ion batteries are of particular interest due to their rechargeability, high energy and power densities, and energy efficiency. Although lithium-ion batteries are now widely used for a variety of applications, their prohibitively high cost has prevented their application in these crucial technologies. For specific applications such as electric vehicles and portable electronics, lithium-ion batteries have yet to achieve the energy and power density requirements necessary, posing additional barriers. On top of these obstacles, the commercial viability of lithium-ion batteries for these applications depends on the ability to scale up the production processes to satisfy the market need, creating yet another challenge for solving these important issues.

While the development of high-capacity anode materials for lithium-ion batteries is a promising route towards enabling these applications, many of the novel designs for such materials are prohibitively expensive or difficult to scale, preventing them from achieving widespread market adoption. In this dissertation, we describe novel materials and processes for producing three high-capacity anode materials of great industry and academic interest: graphene, silicon, and lithium metal. First, we present a novel method for induction heating-mediated synthesis of freestanding anodes for improving the scalability of traditional chemical vapor deposition processes through reduced process downtimes while enabling higher energy and volumetric densities in lithium-ion batteries by virtue of the freestanding nature of the electrode design, reducing the mass and volume of electrochemically-inactive components. Next, we describe a method for the production of silicon/PVA/graphite composite anodes with long cycling life through the use of a 1-step ball milling method utilizing low-cost precursors for scalable production of high-capacity anode materials. Finally, we reveal a design for air-stable lithium metal hosts fabricated from a scalable powder metallurgic approach, which allows for the fabrication of high-performance lithium metal batteries compatible with existing infrastructure, circumventing the need for a high-cost assembly in an inert atmosphere.

The dissertation of Jesse Adam Baucom is approved.

Vasilios Manousiouthakis

Dante Simonetti

Ximin He

Yunfeng Lu, Committee Chair

University of California, Los Angeles

2020

# Table of Contents

# List of Figures

**Chapter 1**

**Chapter 2**

**Chapter 4**

**Chapter 5**

**Chapter 6**

# List of Tables

## Chapter 2

# VITA

| | |
|---|---|
| 2012 – 2016 | B.S., Chemical and Biomolecular Engineering<br>University of Maryland<br>College Park, Maryland |
| 2016 – 2020 | Graduate Researcher, Teaching Assistant<br>Department of Chemical Engineering<br>University of California, Los Angeles<br>Los Angeles, California |

# 1. Background and Motivation

## 1.1 Energy and Our Society

Energy is a fundamental aspect of life, society, and the universe itself. Just like organisms, society has evolved over time to collect, store, and utilize energy more efficiently. During the Agricultural Revolution, the newfound ability to store energy in the form of food lead to a dramatic increase in human population. In more recent times, the Industrial Revolution during the 18th and 19th centuries marked a turning point for our society largely in part to innovations in energy, leading to yet another boom in worldwide population. Society has been and always will be intimately intertwined with our ability to use energy.

Although energy allows us to do more today than ever before, energy has become the driving force for many of our greatest societal challenges. Energy is behind many of the political conflicts that arise today. Unsustainable energy practices raise concerns over the future of our environment. While it may be natural to assume that the solution to fixing such issues is to develop alternative methods for generating and using energy, the ability to effectively store energy may ultimately prove to be key in our global efforts to mitigate such problems.

## 1.2 Climate Change

Over the past century, many studies have revealed the alarming effects that increases in atmospheric temperature may have on our society, including rising sea levels[1], more frequent and violent natural disasters[2], and compromised food security[3]. Although many factors lead to increasing atmospheric temperatures, the general consensus in the scientific community that emissions of "greenhouse gases" such as carbon dioxide ($CO_2$) from human activities contributes to climate change, as evidenced by strong correlations in $CO_2$ emissions, atmospheric $CO_2$ concentrations, and atmospheric temperature over time (Figure 1.1).

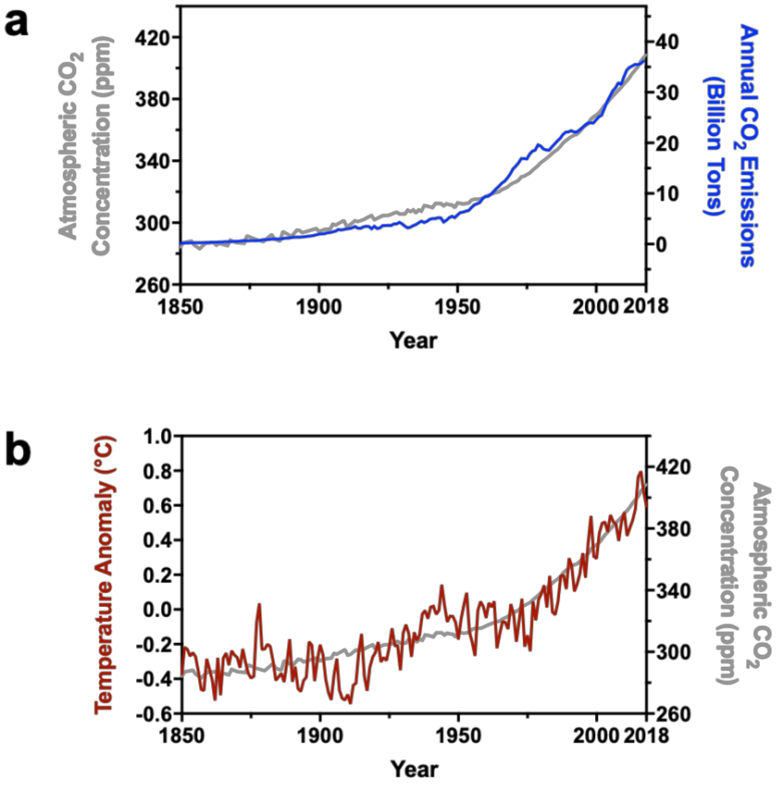

**Figure 1.1** Effect of $CO_2$ emissions on climate. a) Annual $CO_2$ emissions and atmospheric $CO_2$ concentration over time; b) atmospheric $CO_2$ concentration and temperature anomaly over time.[4,5–7]

The main contributors to $CO_2$ emissions are from the energy generation, agriculture, transportation, industry, and residential/commercial sectors (Figure 1.2). With energy generation accounting for over half of the world's $CO_2$ emissions, much of our worldwide efforts to mitigate the effects of global warming is focused on developing renewable energy technologies, constituting any form of energy naturally replenished on a human timescale such as sunlight, wind, rain, tides, waves, and geothermal heat[8]. In order to make the practical transition from fossil fuels to renewable energy, the cost of generating energy from the new source must be competitive with fossil fuels. The levelized cost of electricity (LCOE), defined as the sum of costs over the lifetime of the power plant per unit energy produced over its lifetime, is an indicator for the economic viability of the energy source, where an LCOE approaching that of fossil fuels is more economically viable. As such, our ability to mitigate the consequences of climate change will depend largely on our ability to decrease the cost of renewable energy.

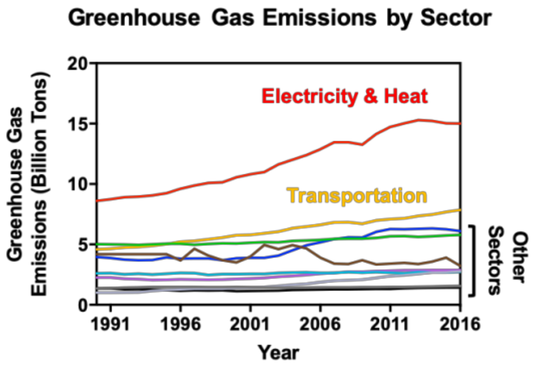

**Figure 1.2** Global $CO_2$ emissions by sector, 1990 – 2016.[4]

## 1.3 Grid Storage

As opposed to fossil fuel-based energy, renewable energy cannot always be produced on demand due to their intermittent nature. As a result, our ability to transition to renewable sources of energy will likely require the use of grid-scale energy storage in order to supply energy during times when energy cannot be generated. Solar photovoltaic (PV) energy, which has gained considerable attention and amassed significant investments over the past few decades, is an attractive source of energy due to the worldwide availability of sunlight and its relatively low LCOE value (Figure 1.3). However, the mismatch in energy demand and energy production rates by solar PV throughout the course of a typical day (Figure 1.4) makes it impossible to fulfill our energy requirements throughout the day without energy storage. Therefore, an appropriate LCOE value for transitioning to solar PV should also incorporate in the price required to store sufficient energy for times when solar energy is unavailable.

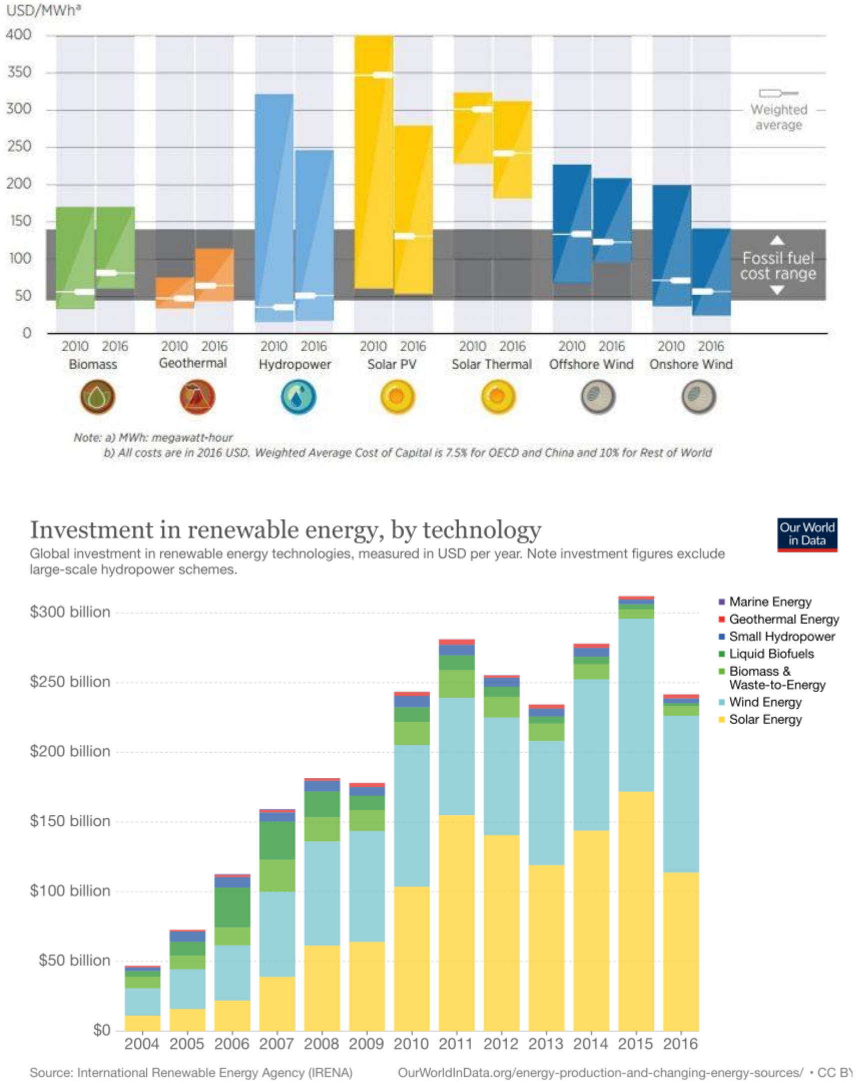

**Figure 1.3** Renewable energy sources. LCOE ranges of various renewable energy sources (top) and investment in renewable energy (bottom).9

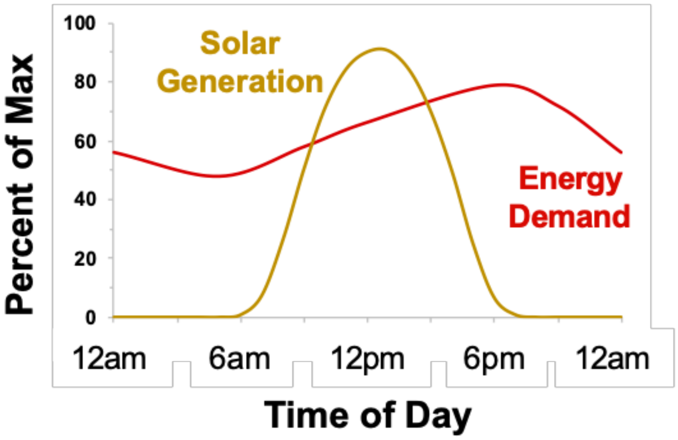

**Figure 1.4** Solar energy generation and energy demand throughout the course of a day. Red line represents energy demand profile in California.[10]

Although lithium-ion batteries represent a potential means for storing the excess energy, the cost of producing enough batteries for grid-scale energy storage is prohibitively large. As a case study, the Hornsdale Power Reserve constructed in 2017 by Tesla in South Australia, consisting of a lithium-ion battery with a capacity of 129 MWh, costed A$90 million, or approximately $65 million USD. In 2019, approximately 30 PWh of energy was consumed in the United States, corresponding to 82 TWh per day[11]. Using the cost per energy of the Hornsdale Power Reserve ($0.50/Wh) and 82 TWh as a crude estimate for the energy storage requirement for complete conversion to solar PV results in a cost of approximately $40 trillion, exceeding the $21 trillion GDP of the United States in 2019. Although the actual cost will ultimately be determined by a wide range of factors, this exorbitant sum highlights the need for a dramatic reduction in the cost of lithium-ion batteries required to transition to renewable energy and avoid the dramatic consequences of climate change.

## 1.4 Electric Vehicles

After energy generation, the transportation sector is the second leading source of global $CO_2$ emissions (Figure 1.2). As a result, governments around the globe are enacting increasing amounts of legislation in order to reduce the effects vehicle emissions, resulting in a dramatic shift of the automotive industry towards electrification. However, widespread adoption of electric vehicles has been inhibited by several issues, most notably the high cost of electric vehicles and various issues concerning the performance of lithium-ion batteries needed for customer satisfaction.

The main performance requirements for commercially-viable electric vehicles is a driving range and recharge time competitive with conventional vehicles. The US Department of Energy and the Advanced Battery Consortium estimated that a driving range of at least 500 km is required, which requires a lithium-ion battery with approximately 235 Wh/kg and 500 Wh/L at the pack level and 350 Wh/kg and 750 Wh/L at the cell level[12]. Furthermore, the pack cost needs to fall below $125/kWh. State-of-the-art automotive lithium-ion battery packs show up to 130-140 Wh/kg and over 210 Wh/L, respectively[13]. Although charging can be done at home overnight, fast charging (reaching at least 80% state-of-charge in 20 min) will still be critical for user acceptance[14].

## 1.5 Portable Electronics

One of the most important outcomes of improvements in cost and performance of lithium-ion batteries is the rise and boom of the portable electronics market. The first mobile phone in 1984 cost over $4,000 and was made from lead-acid batteries attaining a capacity of 500 mAh and a voltage of 7.5 V, allowing for a call of up to 60 minutes on a single charge. The iPhone 11 released by Apple in 2019 used lithium-ion batteries, cost $700 and could stream 10 hours of video on a single charge. Widespread adoption of such devices today was made possible by these improvements in performance and cost, enabling us to do more than ever before and setting a new paradigm for how we communicate with one another.

In accordance with these improvements over time, the market size of the global portable electronics industry is expected to grow to approximately $780 billion in 2023, representing a growth rate of around 8.87% from 2017 to 2023[15]. Correspondingly, the amount of lithium-ion batteries produced for portable electronics is expected to increase from 31 GWh in 2015 to 66 GWh in 2025[16]. This comes as no surprise since current lithium-ion batteries are still far from reaching their theoretical limits in energy density and other performance characteristics, leaving many potential applications waiting for improvements that will ultimately drive this massive market growth.

The electric power industry is a potential beneficiary of the booming lithium-ion batteries industry. On average, utility companies in the United States spend between $6 billion to $8 billion per year to inspect and maintain power lines with helicopters and ground crews[17]. Drones drastically cut the costs of power line inspections for utilities while improving safety, increasing reliability, and reducing response time across transmission and distribution systems. Accessing remote areas of high voltage power lines, either when conducting routine inspections or surveying damage after storms, presents difficult and dangerous obstacles. Drones with long flight ranges and times have the potential to completely eliminate these difficulties and costs, but are at the moment limited by the energy density of lithium-ion batteries. In addition to power line inspections, drones have also been used as a means for restoring data and internet service to areas without access or those losing access. After Hurricane Maria ravaged Puerto Rico and other places in 2017, AT&T launched their own drones to act as cell towers to restore service in areas impacted by the storm, providing cell coverage for up to 8,000 people simultaneously[18]. Perhaps one of the most ambitious applications for drones was revealed in 2013 when Jeff Bezos, CEO and founder of Amazon, announced Amazon Prime Air, the new service for rapid delivery of lightweight commercial products using drones. This application will in part be made possible by the development of lithium-ion batteries with higher energy and power densities allowing for drone-mediated delivery of packages to further distances and of higher weights. As seen by these examples, improvements in lithium-ion batteries has the potential to enable a diverse set of new market opportunities.

# 2. Engineering Principles for Lithium-Ion Batteries

## 2.1 Energy Storage Devices

Among all the different energy storage technologies, capacitors/supercapacitors, batteries, and fuel cells are arguably the most widely used and receive the most interest in academic research. For each application, the choice in energy storage device is typically based on the specific energy and power supplied by the device (Figure 2.1). Capacitors and supercapacitors, which store energy based on capacitance, have high power densities due to their ability to rapidly charge/discharge but typically have low energy densities. Fuel cells, which store chemical energy in the form of fuel, are capable of achieving high energy densities but are limited in power density. With a moderate range of energy and powder densities, batteries provide a “Goldilocks effect” making them useful for a broad range of applications.

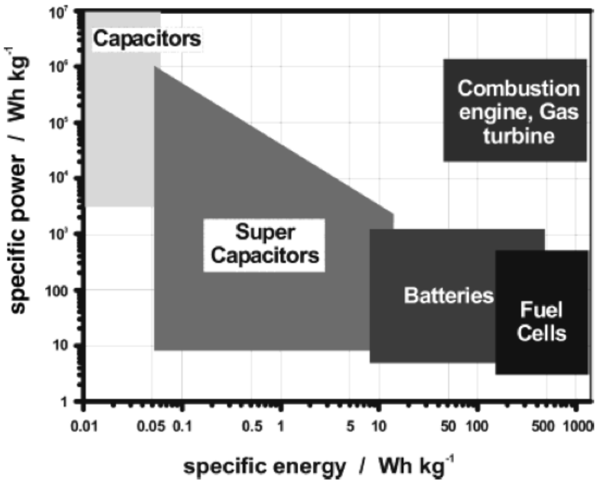

**Figure 2.1** Simplified Ragone plot of various energy storage devices.[19]

## 2.2 Working Principles of Lithium-Ion Batteries

Batteries store energy in the form of electrochemical energy, operating through a pair/sequence of redox reactions in which the electrons coming from the oxidized species are drawn into an external circuit to supply energy before returning to the battery and recombining with the reduced species. Theoretically, batteries can operate using any pair of redox half-reactions. Lithium-ion batteries are those in which lithium ions are the critical species partaking in the redox half-reactions. In comparison to batteries relying on other cell chemistries, including lead-acid and nickel-metal hydride, lithium-ion batteries provide the highest possible energy density and operating voltage by virtue of lithium's low reduction potential (-3.04 V vs the standard hydrogen electrode) and density (0.53 mg/cm$_3$). Additionally, lithium-ion batteries can be recharged hundreds or even thousands of times and possess relatively low rates of self-discharge. For these reasons, lithium-ion batteries are arguably the most useful and have garnered the most attention in industry and academia.

As shown in Figure 2.2, lithium-ion batteries consist of four main components: the cathode, anode, electrolyte, and separator.

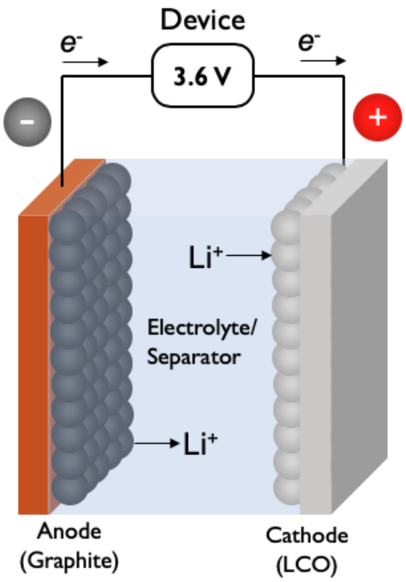

**Figure 2.2** Components and working mechanism of a lithium-ion battery.

*Electrodes*

The cathode and anode are collectively referred to as the electrodes, or the points of the battery where charge enters or exits the battery. During discharge, an electrochemical oxidation reaction occurs at the anode and an electrochemical reduction reaction occurs at the cathode. By convention, electrode in which the electrons leave the battery during discharge is referred to as the negative electrode while the opposite electrode receiving electrons during discharge is the positive electrode. Although the anode and cathode are conventionally defined based on whether the electrode accepts or provides electrodes, it is common in the field of lithium-ion battery research to refer to the negative and positive sides of the battery as the anode and cathode, respectively, regardless of whether the battery is undergoing charge or discharge.

Typical cathode materials for lithium-ion batteries consist of cobalt-based metal oxide particles containing a crystal structure providing sites for the intercalation of lithium ions. When using lithium cobalt oxide (LCO) as the cathode material, the half-reaction at the cathode during discharge is

$$Li^{+} + CoO_2 + e^{-} \rightarrow LiCoO_2$$

where lithium ions ($Li^{+}$) from the electrolyte enter solid particles of $CoO_2$ and recombine with electrons ($e^{-}$) from the external circuit. Typical anode materials for lithium-ion batteries consist of graphite particles, which also provides sites for the intercalation of lithium ions. During discharge, the half-reaction at the anode is

$$LiC_6 \rightarrow Li^{+} + e^{-} + C_6$$

where lithium intercalated within graphite ($LiC_6$) splits into electrons that leave the anode enter the external circuit and lithium ions that diffuse into the electrolyte, leaving behind graphite ($C_6$).

*Electrolyte and Separator*

The electrolyte functions as a $Li^{+}$ conductor and electrical insulator for transporting $Li^{+}$ between electrodes. Typical electrolytes for lithium-ion batteries consist of a polar organic solvent containing a dissolved lithium salt. The solvent used is typically composed of a mixture of carbonate-based liquids such as ethylene carbonate (EC), diethyl carbonate (DEC), or propylene carbonate (PC), whereas the salt used is typically $LiPF_6$. The separator, typically composed of a porous polypropylene membrane, functions solely as an insulating physical barrier between the electrodes to prevent the direct transfer of electrons from within the battery, known as internal short circuiting.

### *Capacity*

The capacity of a battery is determined by the amount of $Li^+/e^-$ pairs that undergo reversible redox reactions within the battery, typically denoted in units of mAh. The amount of $Li^+/e^-$ pairs that can undergo redox reactions is determined by the relative quantities of anode and cathode material. Although every battery has a maximum number of $Li^+/e^-$ pairs that can undergo redox reactions, it is common practice to operate the battery under a shorter depth of charge/discharge in order to prolong the lifetime of the battery; hence, capacity is rated based on the recommended operation windows. The amount of charge stored within each electrode material depends on the amount of $Li^+/e^-$ pairs it can react with. Electrode materials are typically assess based on the capacity per unit mass or volume of host material, referred to as specific capacity and volumetric capacity, respectively. The specific capacity and volumetric capacity are typically reported in units of mAh/g and $mAh/cm^3$, respectively.

### *Voltage*

The voltage of a battery is determined by the difference in electrochemical potential of the reactions at the cathode and anode. Many electrode materials undergo a series of phase changes during lithiation/delithiation, with each phase change possessing a unique electrochemical potential. Although the voltage of a battery is theoretically determined by the potential of each reaction, the operating voltage will typically deviate from such values due to phenomena such as internal resistance, activation polarization, and concentration polarization. Because the voltage of a battery changes throughout the course of charge/discharge, the voltage reported for the battery is typically the average voltage over the course of operation.

### *Energy*

The energy contained in a battery is determined by the product of capacity and voltage of a battery. Much like capacity, energy is typically reported in terms of energy per unit mass or volume, referred to as specific energy and energy density, respectively. Under these considerations, batteries with a high specific energy/energy density will have electrodes with high specific capacities/volumetric capacities, anode materials with low reduction potentials, and cathode materials with high reduction potentials.

### *Rate and Power*

The amount of power provided by a battery is determined by the rate at which the energy of a battery is utilized, which is controlled by the current. The rate at which a battery is charged/discharged is typically quantified in units of C-rate, where a rate of 1 C corresponds to the current density required to complete one full charge/discharge in one hour, 2 C corresponds to the current density required to complete two full charges/discharges in one hour, and C/2 corresponds to the current density required to complete one charge/discharge every two hours. Each battery is typically rated for a specific maximum C-rate, which can be used to determine the specific power of the battery. The power of an electric current is calculated as the product of the current and voltage drop. The specific power of a battery is calculated using the product of the highest current density and the resulting voltage of the battery, with units such as W/kg.

## 2.3 Electrode, Cell, and Pack Assembly

*Electrode Fabrication*

Electrodes are typically constructed by preparing a viscous slurry of electrode particles and a polymeric binder in a solvent and casting the slurry onto a conductive substrate, referred to as the current collector. Conductive additives such as nanoscale particles of carbon, referred to as carbon black, may be added to improve the conductivity of the electrode. After drying off the solvent, the solid particles are bound to the surface of the substrate, which can then be cut into the desired shape. For cathodes, a thin sheet of aluminum is used as the conductive substrate due to its low cost, low density, and high conductivity. Because aluminum, which forms alloys with lithium, is unstable at low electrochemical potentials, copper is used as the conductive substrate for the anode.

*Cell Fabrication*

A single pair of cathode and electrode, constructed with a separator and electrolyte, is referred to as a cell. The voltage of a single cell is determined solely by the electrochemical potential difference between the two electrodes. As shown in Figure 2.3, the cell is fabricated by creating a stack of the anode, separator, and cathode, with electrolyte filling in the void space of the three layers.

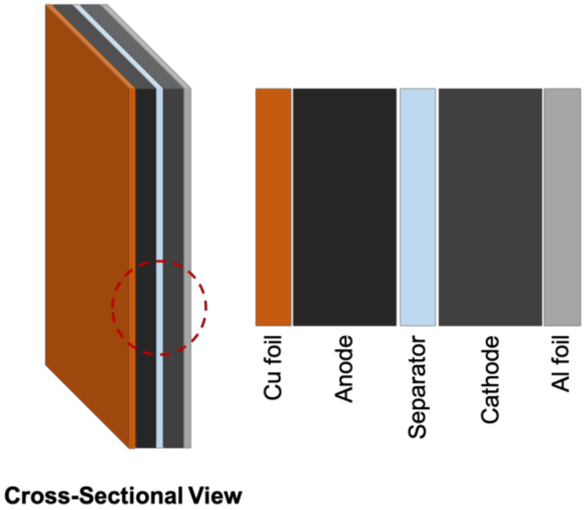

**Figure 2.3** Typical electrochemical cell structure for lithium-ion batteries.

For testing the electrochemical performance of a material used for lithium-ion batteries, it is common practice to construct a coin cell, as shown in Figure 2.4. In order to achieve a high specific energy and energy density, commercial batteries are typically constructed in other configurations, most notably the pouch cell, as shown in Figure 2.5. For pouch cells, the electrode is cast onto both sides of the current collector in order to reduce the mass and volume fraction of non-electrochemically active materials in the battery.

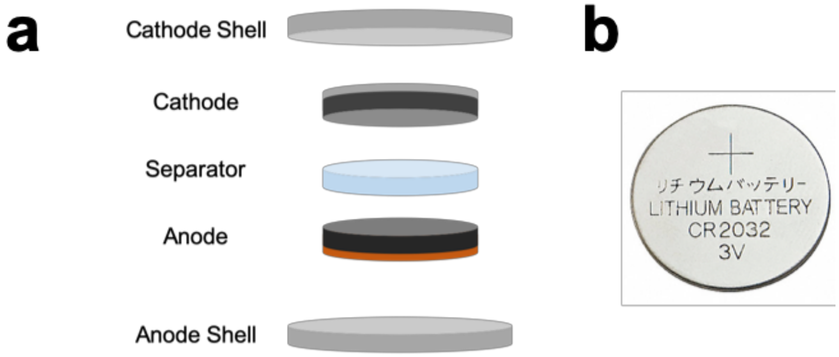

**Figure 2.4** Structure of a coin cell. a) Arrangement of individual components of a coin cell; b) Photograph of a 2032-type coin cell case.

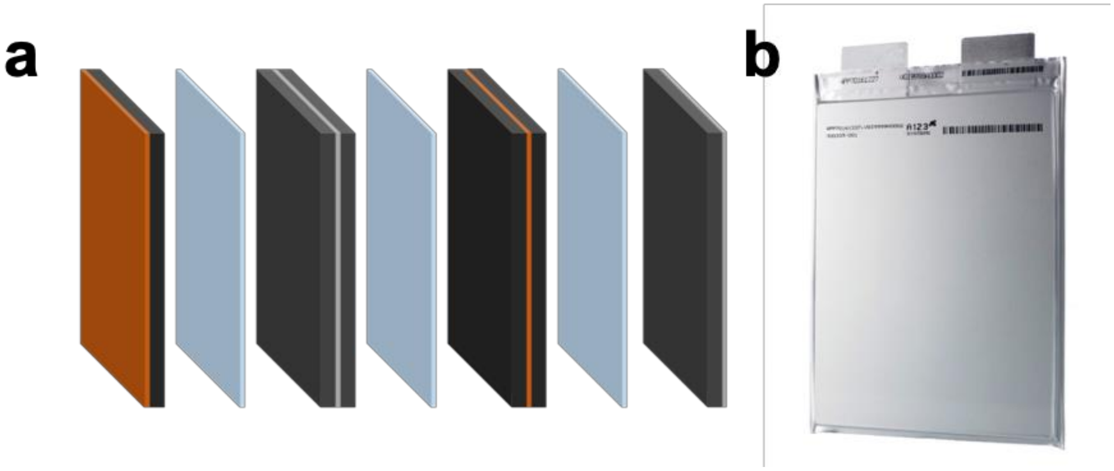

**Figure 2.5** Structure of a pouch cell. a) Arrangement of individual components of a pouch cell; b) Photograph of a pouch cell sleeve.

Due to the requirement of the copper and aluminum current collectors, it is typically desired to prepare thick electrodes in order to reduce the mass and volume fractions of these metals in the batteries, which is crucial for maximizing energy density and minimizing cost. However, thicker electrodes generally lead to diminished performance and shorter lifetimes, indicating that the electrode thickness must be optimized for cell energy/power density and performance. For this reason, the amount of charge that can be stored per unit area of current collector on an electrode, referred to as areal capacity, is a crucial parameter for the design of electrodes.

*Pack Assembly*

Depending on the specific application, cells are arranged in a combination of series and parallel in order to achieve a desired capacity and voltage. In addition to the materials required to create the housing and electrical wiring of the battery pack, a battery management system (BMS) is typically required in order to optimize the performance and lifetime of the battery pack. This requires the BMS to monitor and estimate various parameters of the battery, which may lead to the need for more electrical components, wiring, and housing. Overall, the energy and power densities of the battery pack may fall well below the energy and power densities of individual cells. For many applications, this must be considered when determining the appropriate materials and design that will be implemented on the level of individual cells.

## 2.4 Principles of Anode Materials Design

The critical parameters and characteristics of anode materials of interest are depicted in Figure 2.6. Due to its low cost, low working potential (~ 0.2 V vs. Li/ $Li^+$), and high stability, graphite accounts for around 90% of the market share of anode materials for lithium-ion batteries[20]. Although inferior to graphite in terms of specific capacity, working potential, and cost, lithium titanium oxide (LTO) is featured as an anode material for niche applications due to its superior rate performance and lifetime.

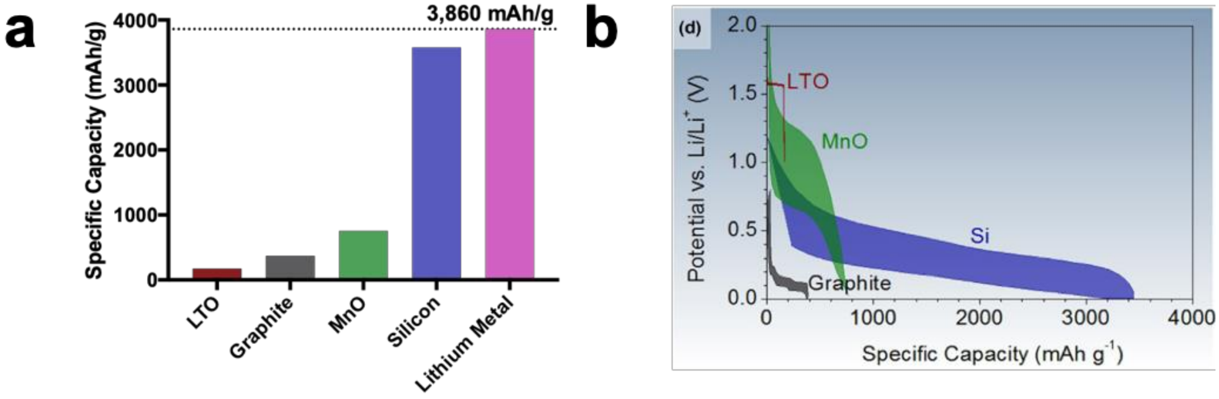

**Figure 2.6** Properties of anode materials of interest. a) specific capacities and b) voltage profiles.[21]

Due to their high specific capacities, silicon and lithium metal represent what are perhaps the most attractive anode materials for next-generation lithium-ion batteries. However, the inferior cycling lifetime of these anode materials and various safety concerns hinders their widespread adoption. Most efforts towards the development of lithium-ion batteries with high energy density are concentrated towards developing silicon- and lithium metal-based anode materials.

During cycling, various phenomena occurring within the battery influence the performance and lifetime of the battery. In order to optimize these characteristics, anode materials must be specially engineered to circumvent various issues that arise as a result of these phenomena.

*Solid Electrolyte Interphase (SEI)*

Anode materials for lithium-ion batteries typically operate at low potentials (close to 0 V vs. Li/Li$^+$). Electrolyte components typically decompose at higher potentials, resulting in the inevitable decomposition of these components on the conductive surfaces of the anode. Such reactions typically consume Li$^+$, reducing the capacity and therefore the lifetime of the battery.

The layer of decomposed electrolyte on the surface of the anode materials is referred to as the solid electrolyte interphase (SEI). Although it consumes $Li^+$, the SEI passivates the surface of the anode, inhibiting further side reactions and improving lithium transport kinetics between the electrolyte and electrode particles. As an electrically insulating surface, the SEI also contributes to increases in impedance, potentially resulting in lower operating voltages and capacities.

The coulombic efficiency (CE) is the ratio of discharge capacity versus charge capacity for a given cycle, where side reactions such as formation of SEI result in lower CEs. Since batteries are typically prepared with no charge in the anode, the SEI is initially formed during the very first charge, resulting in a low CE value for the first cycle. For this reason, the initial coulombic efficiency (ICE) is another critical parameter. Since SEI formation is considered unavoidable for conventional lithium-ion batteries, extra cathode is typically added to compensate for $Li^+$ loss during the first cycle. Because SEI is formed on the surface of the anode particles, specific surface areas typically result in higher ICEs. For subsequent cycles, it is desired to minimize the formation of new SEI in order to maximize the CE and lifetime of the battery. To achieve this, the anode material must be designed to minimize the fracture of the SEI and formation of new electrode/electrolyte interfaces. Although this issue is not very prevalent for traditional anode materials, it is extremely problematic for materials capable of storing large quantities of lithium due to the associated structural changes, compromising the integrity of the SEI.

### *Pulverization*

Due to the dynamic processes that occur during cycling, it is possible for electrode particles to become electrically isolated from the battery, reducing the amount of material that can store $Li^+$.

In addition to excessive SEI formation, electrical isolation can occur as a result of irreversible changes to the electrode structure caused by volumetric expansion or cracking of electrode particles. In order to mitigate these issues, the materials and electrodes must be designed in such a way to retain electrical conduction among all particles as well as possible.

### *Electrical and Ionic Conductivity*

The transport of $Li^+$ and electrons are crucial aspects for lithium-ion battery performance. Anode materials should be designed in such a way to maximize their electrical conductivity in order to reduce the voltage drop caused by ohmic resistance. Additionally, most anodes require the diffusion of $Li^+$ throughout the volume of the material in order to achieve complete electrochemical lithiation. As a result, materials with low $Li^+$ diffusivity will result in concentration polarization, which also results in lower working potentials and capacities. These phenomena become more crucial for applications requiring larger power densities since larger currents are necessary to meet these requirements. In order to improve $Li^+$ transport kinetics, shorter diffusion lengths are desired, although this typically requires smaller particles sizes, conflicting with the need for larger particles in order to maximize ICE. As a result, particle size and structure must typically be optimized in order to achieve an appropriate trade-off in ICE and rate performance.

## 2.5 Performance Limitations of Current Anode Materials

### *Electric Vehicles*

As previously mentioned, widespread adoption of electric vehicles is likely only possible if lithium-ion battery packs reach 235 Wh/kg and 500 Wh/L at the battery pack level and 350

Wh/kg and 750 Wh/L at the cell level[12]. Estimated energy densities and specific energies of various anode/cathode pairs are depicted in Figure 2.7. Although on the material level graphite can fulfill these specific energy and energy density requirements, the necessity for additional components such as current collectors and separators renders it insufficient for electric vehicles, as indicated by the estimations.

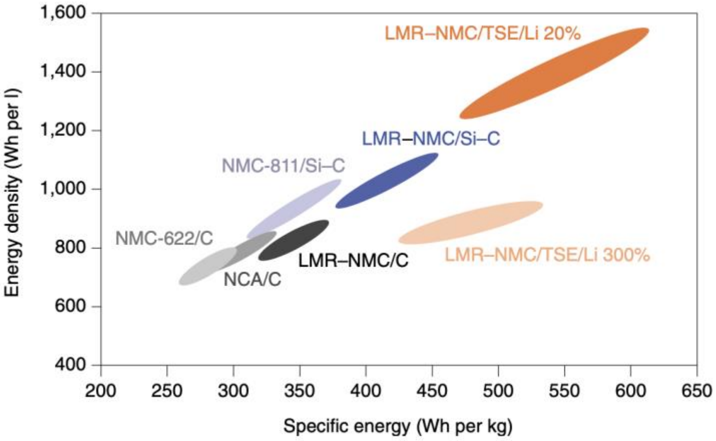

**Figure 2.7** Energy density and specific energy of different cell chemistries at electrode stack level. The ellipses are based on the calculation of different values for positive electrode thicknesses, ranging from 50 µm up to 150 µm. Si-C estimates are based on a silicon-carbon composite containing 20% silicon.[14]

Although increasing the specific capacity of the anode or cathode will improve the overall energy density of the battery, the technological maturity of current cathode materials combined with the lack of viable alternatives under research has directed efforts in increasing battery energy densities towards the development of high-capacity anode materials. An overview of the different lithium-ion battery chemistries used for various battery packs for electric vehicles is listed in Table 2.1. In general, battery packs consisting of graphite-based anodes typically fall far short of the 235

Wh/kg and 500 Wh/L goals. The batteries for the Tesla Model X and Tesla Model 3 have attained these energy requirements both contain small amounts of silicon in the anode, highlighting the need for high-capacity anode materials for achieving the necessary performance characteristics.

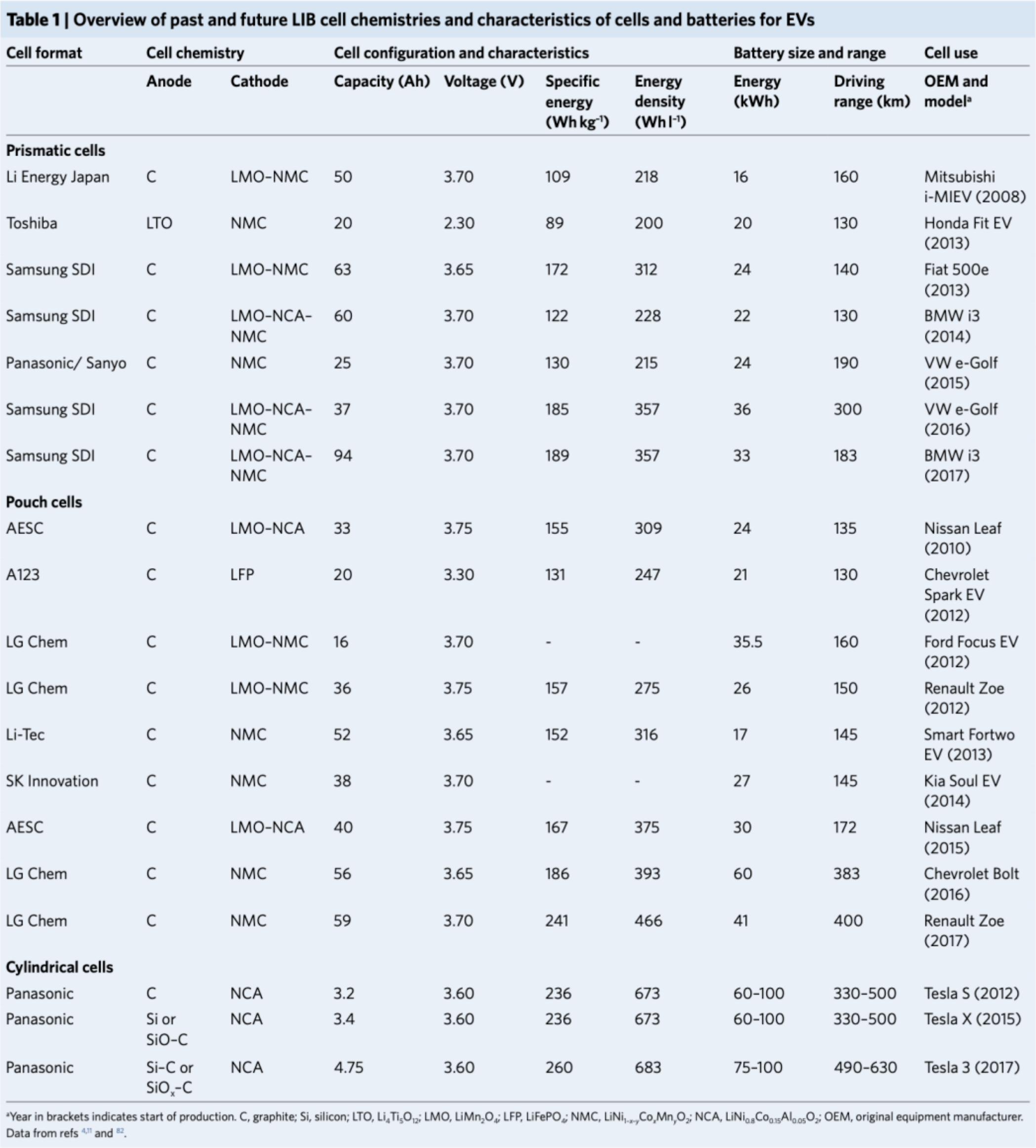

**Table 1 | Overview of past and future LIB cell chemistries and characteristics of cells and batteries for EVs**

| Cell format | Cell chemistry | | Cell configuration and characteristics | | | | Battery size and range | | Cell use |
|---|---|---|---|---|---|---|---|---|---|
| | Anode | Cathode | Capacity (Ah) | Voltage (V) | Specific energy (Wh kg$^{-1}$) | Energy density (Wh l$^{-1}$) | Energy (kWh) | Driving range (km) | OEM and model[a] |
| **Prismatic cells** | | | | | | | | | |
| Li Energy Japan | C | LMO-NMC | 50 | 3.70 | 109 | 218 | 16 | 160 | Mitsubishi i-MIEV (2008) |
| Toshiba | LTO | NMC | 20 | 2.30 | 89 | 200 | 20 | 130 | Honda Fit EV (2013) |
| Samsung SDI | C | LMO-NMC | 63 | 3.65 | 172 | 312 | 24 | 140 | Fiat 500e (2013) |
| Samsung SDI | C | LMO-NCA-NMC | 60 | 3.70 | 122 | 228 | 22 | 130 | BMW i3 (2014) |
| Panasonic/ Sanyo | C | NMC | 25 | 3.70 | 130 | 215 | 24 | 190 | VW e-Golf (2015) |
| Samsung SDI | C | LMO-NCA-NMC | 37 | 3.70 | 185 | 357 | 36 | 300 | VW e-Golf (2016) |
| Samsung SDI | C | LMO-NCA-NMC | 94 | 3.70 | 189 | 357 | 33 | 183 | BMW i3 (2017) |
| **Pouch cells** | | | | | | | | | |
| AESC | C | LMO-NCA | 33 | 3.75 | 155 | 309 | 24 | 135 | Nissan Leaf (2010) |
| A123 | C | LFP | 20 | 3.30 | 131 | 247 | 21 | 130 | Chevrolet Spark EV (2012) |
| LG Chem | C | LMO-NMC | 16 | 3.70 | - | - | 35.5 | 160 | Ford Focus EV (2012) |
| LG Chem | C | LMO-NMC | 36 | 3.75 | 157 | 275 | 26 | 150 | Renault Zoe (2012) |
| Li-Tec | C | NMC | 52 | 3.65 | 152 | 316 | 17 | 145 | Smart Fortwo EV (2013) |
| SK Innovation | C | NMC | 38 | 3.70 | - | - | 27 | 145 | Kia Soul EV (2014) |
| AESC | C | LMO-NCA | 40 | 3.75 | 167 | 375 | 30 | 172 | Nissan Leaf (2015) |
| LG Chem | C | NMC | 56 | 3.65 | 186 | 393 | 60 | 383 | Chevrolet Bolt (2016) |
| LG Chem | C | NMC | 59 | 3.70 | 241 | 466 | 41 | 400 | Renault Zoe (2017) |
| **Cylindrical cells** | | | | | | | | | |
| Panasonic | C | NCA | 3.2 | 3.60 | 236 | 673 | 60-100 | 330-500 | Tesla S (2012) |
| Panasonic | Si or SiO-C | NCA | 3.4 | 3.60 | 236 | 673 | 60-100 | 330-500 | Tesla X (2015) |
| Panasonic | Si-C or $SiO_x$-C | NCA | 4.75 | 3.60 | 260 | 683 | 75-100 | 490-630 | Tesla 3 (2017) |

[a] Year in brackets indicates start of production. C, graphite; Si, silicon; LTO, $Li_4Ti_5O_{12}$; LMO, $LiMn_2O_4$; LFP, $LiFePO_4$; NMC, $LiNi_{1-x-y}Co_xMn_yO_2$; NCA, $LiNi_{0.8}Co_{0.15}Al_{0.05}O_2$; OEM, original equipment manufacturer. Data from refs [4,11] and [82].

**Table 2.1** Overview of lithium-ion battery cell chemistries and characteristics of cells and batteries for electric vehicles.[14]

## 2.6 Cost of Lithium-Ion Batteries

As previously mentioned, a cost of $125/kWh is necessary for commercially viable electric vehicles. The large number of complex processes required for the manufacture of lithium-ion batteries create a diverse set of factors contributing to cost. In general, the costs can be broken down into the material costs and operating costs, with the much of the material costs coming from the cell components. Overall costs and material costs for lithium-ion battery packs are depicted in Figure 2.8. Note that material costs account for most of the total costs for battery production. The estimations reported for material costs are based on the cost of the raw materials required and does not factor on costs for additional material processing steps, which likely lead to significantly larger costs. Therefore, although on the material level it is possible to achieve costs near $70/kWh, the total material and manufacturing costs in 2016 was around $200/kWh, suggesting that significant improvements are necessary to the goal of $125/kWh.

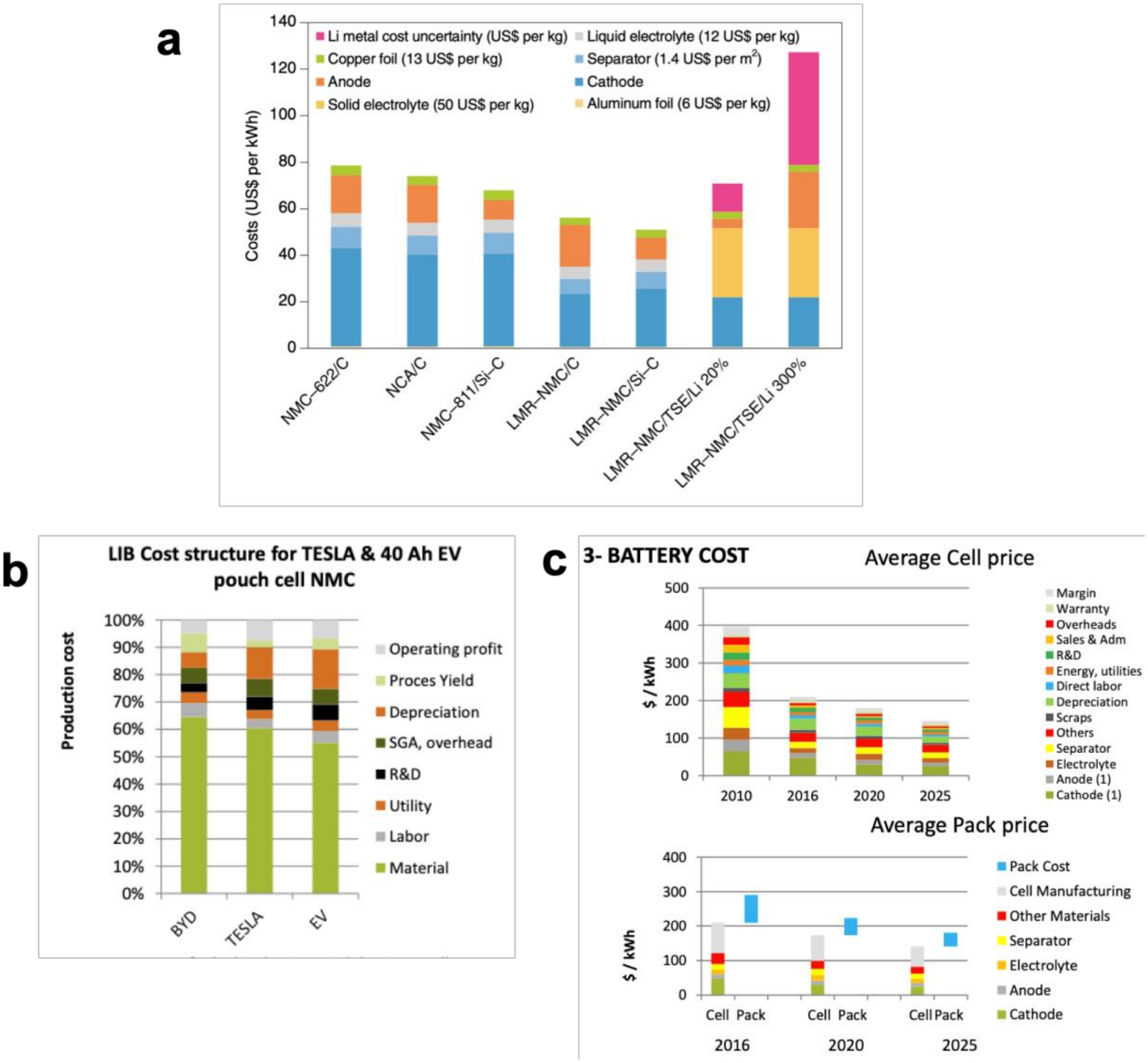

**Figure 2.8** Cost of lithium-ion battery packs for electric vehicles. a) Raw material costs for different cell chemistries at electrode stack level[14]; b) Cost structure for lithium-ion battery cells in electric vehicles[22]; c) Cost per kWh of lithium-ion battery cells and packs over time[22].

# 3. Thesis Objectives

## 3.1 Thesis Objectives

Although all components of lithium-ion batteries are constantly undergoing improvements, the development of high-capacity and cost-effective anode materials is an area of particular interest. Novel anode materials with high volumetric capacity, high specific capacity, and fast charging capabilities results in batteries with higher specific energy, energy density, and power densities, improving current applications and enabling new applications. At the same time, the development of novel processes enabling large-scale production of anode materials is necessary to fulfill the market need. Under these considerations, the objective of this thesis is as follows:

1) Develop novel anode materials with higher specific capacity than current industry standards
2) Develop high-performance anode materials from scalable processes
3) Develop novel processes for the production of anode materials for reducing material costs, reducing battery fabrication complexity, and improving process scalability
4) Provide new perspectives and insights for the development of novel materials and processes for anode materials with high specific capacity and energy density and batteries in general

## 3.2 Outline of Research Work

The following sections will present three different projects for the development of scalable, low-cost anode materials for next-generation lithium-ion batteries. As previously mentioned, graphite is the anode material of choice for most applications, but many other anode materials are under investigation in academia and industry for lithium-ion batteries with high energy density. Of these materials, graphene, silicon, and lithium metal are of particular interest due to their high theoretical capacities of 744 mAh/g, 3,579 mAh/g, and 3,860 mAh/g, respectively. The three projects presented in this thesis will feature graphite, silicon, and lithium metal as the active material in the newly developed anode material. For each project, information on the state-of-the-arts, the results of the research work, and potential directions for future work will be discussed.

# 4. Freestanding Graphene Anodes Synthesized via Induction Heating-Mediated Chemical Vapor Deposition for Scalable, High Energy Density Lithium-Ion Batteries

## 4.1 Introduction

Graphite, with a theoretical specific capacity of 372 mAh/g, is the current anode material of choice, comprising approximately 90% of the market share of lithium-ion battery anodes[20]. Although graphite exhibits excellent electrochemical stability, the low diffusivity of $Li^+$ in graphite paired with the need for a large particle size for a sufficiently high ICE makes it inadequate for applications demanding high current densities. Further complicating this issue is the phenomena of lithium dendrite growth on the surface of graphite particles under fast charging conditions as a result of the relatively low lithiation potential, potentially leading to rapid capacity decay, internal short circuiting, and thermal runaway. As a result, tremendous efforts have been exerted into developing alternative materials with superior capacity and rate performance.

Graphene, with a theoretical specific capacity of 744 mAh/g, holds great promise as an anode material superior to graphite. With twice the theoretical specific capacity, graphene enables applications requiring high specific capacity in which graphite is inadequate. Additionally, due to its unique structural properties, graphene provides low-resistance pathways for lithium transport, making it ideal for applications requiring high current densities. Despite great promise, graphene has yet to become commercially viable due to several issues, most notably the difficulty in scaling processes for graphene synthesis. Improving the scalability of graphene synthesis processes is key for enabling widespread adoption and improving the energy and power densities of lithium-ion batteries.

## 4.2 Principles of Graphitic Carbon Anodes

*Structure and Composition*

Graphene is a two-dimensional sheet of carbon atoms arranged in a hexagonal lattice where all carbons are bonded via $sp^2$ bonds. As a result of this chemical arrangement, graphene possesses outstanding electrical conductivity (up to $10^8$ S/m)[23], mechanical strength (Young's modulus of 2 TPa)[24], and flexibility, providing a unique set of characteristics making it useful for a diverse array of applications. Graphite is a three-dimensional material composed of stacks of individual sheets of graphene, representing the most stable form of carbon under standard conditions. Although ideal graphite and graphene are composed entirely of carbon atoms, defects are inevitably found throughout the material, making it common to find atoms such as hydrogen and oxygen. Additionally, carbon atoms can be substituted for atoms such as boron and nitrogen while preserving the hexagonal arrangement of atoms, endowing the material with unique properties deviating from those of ideal graphene.

Although lithium cannot diffuse through individual sheets of defect-free graphene, lithium can diffuse between layers of graphene within graphite, as well as through defects in individual planes of graphene. The relatively low diffusivity of lithium in graphite ($10^{-11} – 10^{-7}$ $cm^2/s$)[21] results from the close packing of adjacent sheets of graphene that provide narrow diffusion channels requiring high activation energies for diffusion. Under this consideration, the diffusivity of lithium can theoretically be improved by widening the spacing between individual sheets of graphene in graphite, as well as by reducing/preventing stacking of graphene sheets. Because ideal graphene is composed of individual sheets of carbon rather than stacks of carbon sheets, graphene possesses much lower barriers for lithium diffusion, allowing it to charge/discharge under larger current densities without sacrificing specific capacity. Note that although graphene is ideally a single sheet of carbon, essentially all graphene synthesis methods result in a small degree of stacking. Nevertheless, this phenomenon does not prevent graphene from achieving the aforementioned advantages in specific capacity and rate performance.

### *Lithium Storage Mechanisms*

During lithiation, lithium and graphite undergo phase changes with voltage plateaus of 0.07, 0.10, and 0.19 V upon lithiation and 0.1, 0.14, and 0.23 V upon delithiation[21]. The fully lithiated state of graphite is $LiC_6$, in which lithium is intercalated between individual sheets of graphene. Although this intercalation mechanism results in a relatively low specific capacity of 372 mAh/g, many have reported abnormal lithium storage mechanisms for partially graphitic or disordered carbon materials, occasionally leading to specific capacities higher than the theoretical capacity of pure graphite (Figure 4.1). One report found that a slightly extended interlayer spacing (4 Å) between graphene layers allowed the formation of $Li_2$ molecules intercalated in graphite, thereby increasing its lithium storage capability[25]. Additional reports have suggested that lithium atoms may be stored within mesoporous cavities in carbon[26] or the edges and surfaces of individual sheets of graphene, resulting in specific capacities much higher than graphite's theoretical value[27,28]. As a result of these favorable phenomena, great effort has been directed towards the development of graphene-based anode materials with specially tailored structures enabling the storage of excess lithium through such mechanisms.

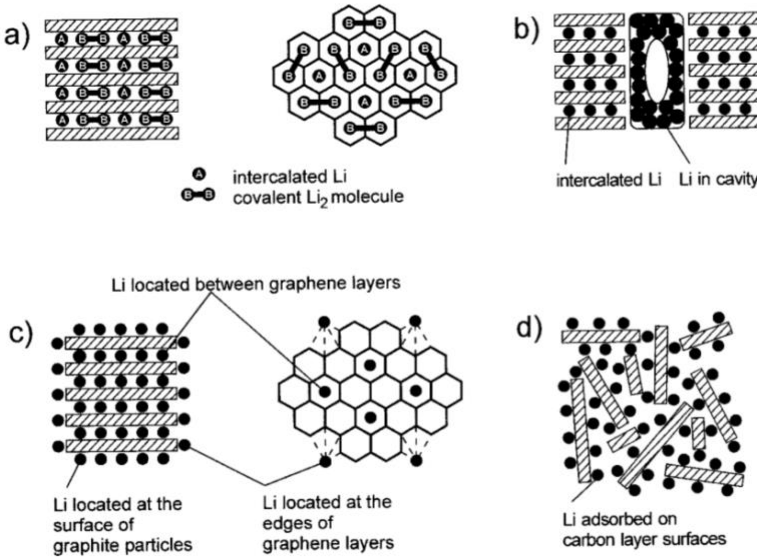

**Figure 4.1** Hypothesized lithium storage mechanisms in high-capacity carbon-based materials reported in the literature. a) intercalation of lithium between layers of graphene; b) lithium storage in microporous cavities; c) lithium adsorption on edge sites; d) lithium adsorption on surfaces.[29]

*Lithium Dendrite Growth*

Although the low lithiation/delithiation potential of graphite endows full cells with a high working potential, it encourages the formation and growth of lithium metal deposits, leading to several negative consequences. The low lithiation potential of graphite combined with the low lithium diffusivity in graphite makes results in high overpotential at elevated rates, resulting in even lower lithiation potentials that encourage nucleation of lithium metal deposits on the surface of graphite particles. Furthermore, overcharging graphite results in the deposition of lithium metal on the surface due to the lack of intercalation sites, often making it necessary to add excess anode to batteries to avoid this issue. After the nucleation of lithium metal, further plating of lithium becomes easier due to the lower energy barrier for lithium metal deposition on metallic lithium in comparison to graphite. Under this condition, rapid capacity decay may occur as a result of the formation of new electrode/electrolyte surfaces that consume electrolyte to form more SEI. Perhaps the most critical consequence of this phenomenon is the potential for lithium dendrites to grow far enough to extend to the cathode, resulting in an internal short circuit that causes thermal runaway and inflammation of the liquid electrolyte, posing serious safety concerns. For these reasons, charging rates of graphite anodes must be sufficiently low and carefully controlled in order to prevent lithium dendrite formation and growth.

## 4.3 State-of-the-Arts

*Commercial Processes for Graphite Synthesis*

As the most stable form of carbon under standard conditions, graphite forms naturally as a result of the reduction of carbonaceous precursors, typically dead organisms, hence the term "fossil fuels" used to describe graphite and similar materials in reference of this phenomenon. Although natural graphite can be used as anode materials after refinement, graphite can also be produced synthetically from carbonaceous precursors (Figure 4.2). To produce synthetic graphite, carbonaceous precursors such as coke is calcinated at 800 – 1,200 °C into a graphitizable carbon material referred to as soft carbon. After grinding the soft carbon into the desired size, the material is processed at temperatures exceeding 2,500 °C for several days to weeks, including cooling steps, to produce graphitized carbon. Finally, the graphitized particles are grinded, coated, and optimized for particle size design to achieve the desired anode performance[30–33]. To make natural graphite suitable for lithium-ion batteries, the flaky graphite precursors must be separated and concentrated by methods such as flotation[31,32,34]. Through this process, purity levels of around 95% can be achieved, with the main impurities consisting of silicate mineral grains and chemical compounds of S, K, and Na, among others. The resulting graphite flakes are treated by sophisticated milling techniques to obtain spherical particles in the micrometer range and subsequently undergoes wet-chemical and/or thermal purification processes, most likely by leaching with hydrofluoric acid or thermal treatment at over 2,000 °C to decrease the impurity content to less than 500 ppm. Similar to synthetic graphite processing, the particles are refined via grinding, coating, and optimization of size[32].

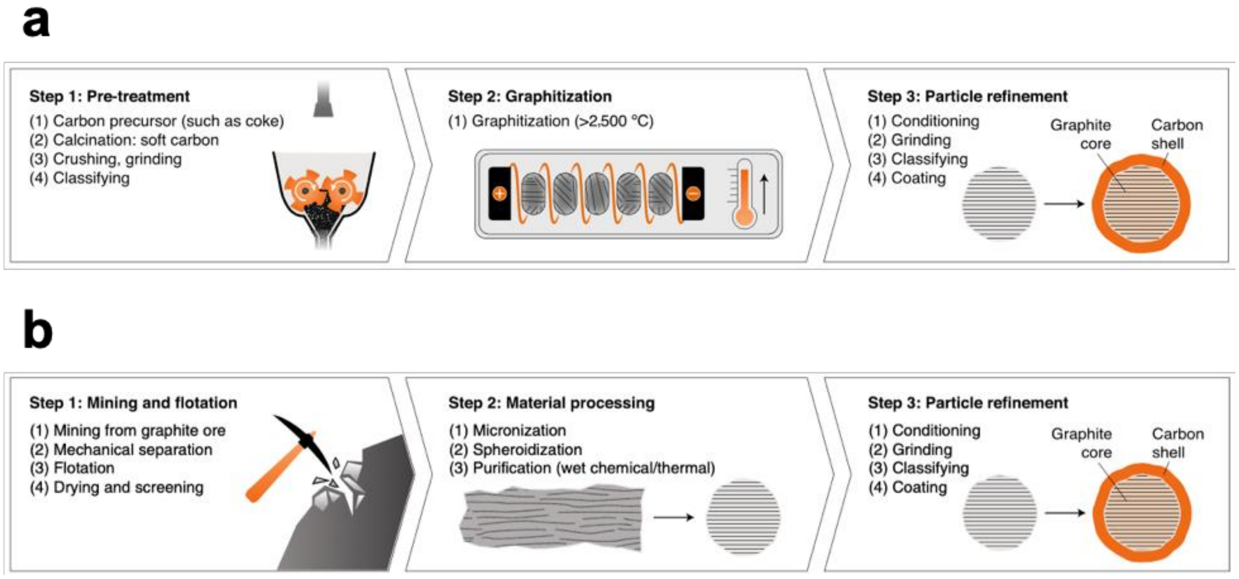

**Figure 4.2** Production of a) synthetic and b) artificial graphite.[14]

As a result of the low cost of the material precursors and extreme temperatures required for graphite production, most of the material costs are energy costs during graphitization[22]. As of 2016, the price for natural graphite amounts to around $8 per kg, while the price of synthetic graphite is around $13 per kg. Despite its low cost, natural graphite has been deemed a critical, strategic material by the United States and governments in Europe. In anticipation of potential supply bottlenecks for natural graphite, great effort has been made to reduce the cost of synthetic graphite, which is expected to decrease to below $10/kg in 2025.

### *Graphene Synthesis*

In general, graphene is synthesized through two approaches: top-down, and bottom-up. In the top-down approach, graphite is exfoliated into individual sheets of graphene through various physical or chemical means. A popular method for graphite exfoliation is through the oxidation of graphene to produce water-soluble oxygen-containing functional groups such as epoxides or hydroxyls.[35] The resulting material, referred to collectively as graphene oxide (GO), can be subsequently converted back to graphene through thermal treatment. The final material is often referred to as reduced graphene oxide (rGO) to more accurately describe its chemical structure. Despite the fact that graphene can be produced in relatively large quantities through this method, rGO typically contains an abundance of defects due to the harsh chemical and thermal processing conditions necessary to introduce and remove oxygen from the material, making it unsuitable for many applications.

In the bottom-up method, graphene is synthesized from carbonaceous small molecules or polymer precursors.[36] While typical graphitization is done at temperatures exceeding 2,000 °C, catalysts can be used to produce high-quality graphene at moderate temperatures (800 – 1,000 °C). Chemical vapor deposition (CVD) is perhaps the most popular method for bottom-up synthesis of graphene. Typically, the process is done by creating a catalyst template for graphene growth such as copper, nickel, or magnesium oxide and heating the template in a furnace under the flow of a carbonaceous precursor such as methane. Using this method, graphene with specifically designed architectures can be produced by careful design of the catalyst template. A recent study by Mo et al. revealed that mesoporous graphene grown via CVD on a porous magnesium oxide (MgO) template attained a specific capacity of 1,182 mAh/g at 0.2 C while still maintaining a capacity of

440 mAh/g at a rate of 60 C, demonstrating both high capacity and fast charging capability[37]. Although this study elucidates the high potential for graphene as anode materials in lithium-ion batteries, large-scale adoption of graphene grown by CVD is currently infeasible due to the small batch sizes and long processing times. Significant improvements in the scalability of CVD is therefore necessary in order to enable large-scale application of graphene anodes.

## 4.4 Design and Process Overview

In order to enable large-scale replacement of graphite anodes with superior graphene anodes, modifications in the CVD must be made to increase material production rates. One key barrier limiting the scalability of CVD is the long downtimes associated with heating/cooling. Although the actual reaction typically takes place on the order of minutes, CVD processes are typically carried out at temperatures around 800 – 1,000 °C, typically requiring long periods of time for heating and cooling on the order of minutes to hours.

To address this issue, we herein describe a novel method for induction heating-mediated CVD. Induction heating refers to the phenomena in which a material surrounded by an electric coil with a large alternating current is heating via electromagnetic induction. Following Lenz's law, the induced magnetic field induces an opposing magnetic field in the material within the coil in the form of Eddy currents, causing the sample to heat due to Joule heating. An important aspect of the process is the fact that heat is not transferred by conduction but generated within the target material itself, which helps significantly reduce heat dissipation and improve the energy efficiency of the heating process. Furthermore, the heating and cooling processes occur on the order of seconds to minutes, significantly reducing process downtimes, enabling a higher output of graphene production.

A schematic illustration of the process is depicted in Figure 4.3. Porous nickel templates were first prepared via compaction of nickel microparticles followed by light annealing to form a three-dimensional nickel template (3D-Ni). CVD was then done on the 3D-Ni template using acetonitrile as the carbon source and induction heating as the heat source to form N-doped graphene over the catalyst surface. The resulting N-doped graphene-coated 3D-Ni was then etched to remove nickel, forming three-dimensional N-doped graphene (3D-NG).

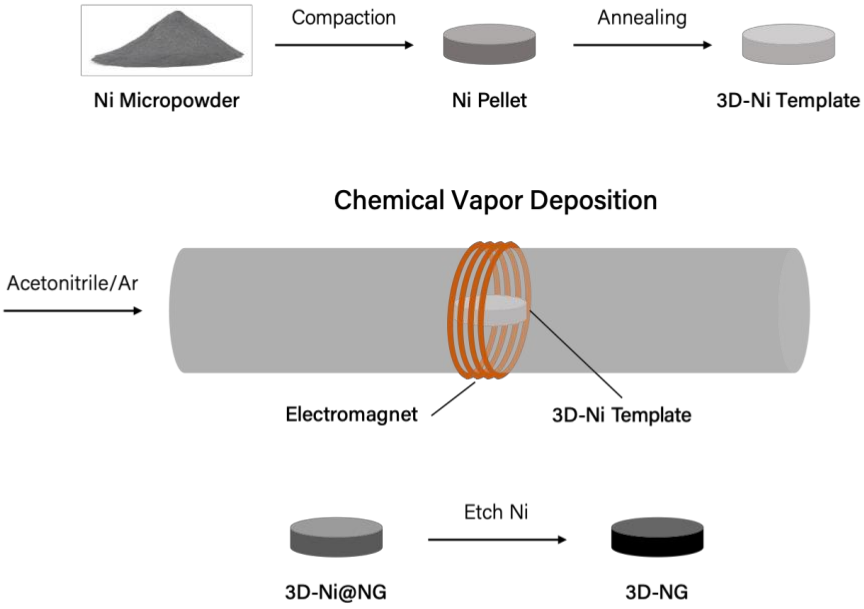

**Figure 4.3** Schematic illustration of 3D-NG synthesis.

## 4.5 Methods

*Preparation of Nickel Catalyst Template*: In a typical synthesis, 200 mg nickel particles were pressed into a disc-shaped pellet with a diameter of 13 mm using a weight of 0.35 T. The pellets were then heat treated in a tube furnace at 900 °C for 10 min under the flow of argon containing 5 mol% $H_2$. This process could theoretically also be done using induction heating as the heat source in order to improve the energy efficiency and lower the overall process time. The resulting pellet typically had a diameter of 11 mm and a thickness of 650 μm.

*Induction Heating-Mediated Chemical Vapor Deposition*: Using induction heating as the heating source, chemical vapor deposition was then performed on the nickel template using acetonitrile as the nitrogen-containing carbon source. A stream of pure argon with a flow rate of 1 SLPM was bubbled through acetonitrile in a heating mantle set to 60 °C to carry acetonitrile vapors into the heating zone. Induction heating was performed with an electromagnet for a total of 10 minutes from the time the induction heating began to the time when induction heating stopped. After heating, the pellet was allowed to cool down to room temperature naturally. The resulting pellet was composed of a three-dimensional nickel network coated with graphene, denoted 3D-Ni@NG.

*Removal of Nickel Template*: Nickel was then chemically etched from 3D-Ni@NG using a modified version of a previously reported protocol (ref from 3D-G@PDMS paper). 3D-Ni@NG was first immersed in a solution of 4% poly(methyl methaceylate) (PMMA) ($M_w$ = 996,000) in ethyl acetate. After removing the pellet from the PMMA solution, the excess solution was dried in air and baked at 180 °C for 30 min to coat the material in PMMA. The pellet was subsequently immersed in a solution of 1 M HCl at 70 °C overnight to remove the nickel template. After washing the pellet with water three times, the PMMA was removed by immersing the pellet in hot (50 °C) acetone for 1 h. The resulting material was dried in air at room temperature, followed by drying in a 70 °C vacuum oven for 1 day to yield 3D-NG.

*Materials Characterization:* XRD spectra were obtained with a Rigaku powder X-ray diffractometer (XRD) using Kα radiation (λ = 1.54 Å). Transmission electron microscopy (TEM) images were obtained with Titan S/TEM scanning transmission electron microscope (FEI). Scanning electron microscopy (SEM) images were taken with a Nova 230 Nano SEM. Raman spectra were obtained with a Renishaw 2000 System with a He/Ne laser at a wavelength of 633 nm. Thermogravimetric analysis (TGA) was performed in air using a ramp rate of 10 $_{o}$C min$_{-1}$. Gas sorption measurements were conducted using a Micromeritics ASAP 2020 system at 77 K. Prior to gas adsorption/desorption measurement, all power was degassed at 120 °C for 12 h.

*Coin Cell Assembly:* Electrodes were prepared by cutting the as-prepared 3D-NG sheets into the desired shape. Half-cells were assembled using 2032-type coin cells using Li foil as the counter/reference electrode, 1 M $LiPF_6$ in a mixture of ethylene carbonate (EC)/dietyl carbonate (DEC) containing 5 vol% fluoroethylene carbonate (FEC) as the electrolyte, and porous polypropylene separators.

*Electrochemical Characterization:* Electrochemical impedance spectroscopy (EIS) measurements were taken using an amplitude of 100 mV and frequencies ranging from 100 kHz to 10 mHz. Cycling performance was conducted with a LAND battery testing system (China). Specific capacities were calculated based on the total mass of the active material.

## 4.6 Results and Discussion

*Heating Profile*

The temperature profile of a typical induction heating process is presented in Figure 4.4. The data shown represents the heating profile used for 1 min of heating at 800 °C. Using induction heating, a temperature of 750 °C is reached within 30 seconds, surpassing 800 °C within 45 seconds. For a CVD process in a tube furnace and a heating rate of 20 °C, a sample starting at 40 °C with a target CVD temperature of 800 °C would take 38 minutes to heat up, corresponding to a 50-fold drop in heating time required for the induction heating process. In addition to reduced process downtimes, induction heating enables higher energy efficiency than traditional CVD while marking a significant decrease in energy costs in comparison to traditional graphite synthesis processes, which typically require several days or weeks of heating at temperatures exceeding 2,500 °C.

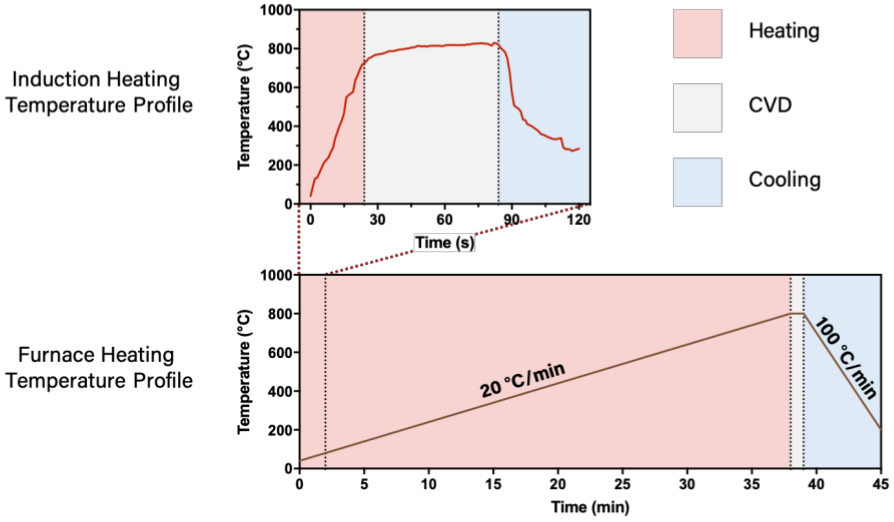

**Figure 4.4** Heating profiles of CVD performed with induction heating and a conventional tube furnace. In both cases, CVD time and temperature are 1 min and 800 °C, respectively.

### *Materials characterization*

Morphological characterization of 3D-NG is displayed in Figure 4.5. SEM imaging reveals that the precursor nickel particles (Figure 4.5a) possess spiky surface morphology and a size of 2 – 3 µm. After annealing the nickel particles together and conducting CVD, the resulting 3D-NG (Figure 4.5b), displays an interconnected sponge-like structure with pores sizes on the range of microns. The precursor nickel template, containing a mass of 200 mg, height of 650 µm, and diameter of 11 mm, corresponding to a volume of 62 mm$_3$, has a theoretical void fraction of 0.64 based on a density of 8.91 mg/mm$_3$ for nickel. The large void fraction allows for diffusion of acetonitrile throughout the volume of the nickel template during the CVD process. Although a large void volume theoretically leads to a low volumetric capacity, 3D-NG can be compressed to more than 10 times its original thickness without fracture by virtue of the outstanding flexibility of graphene. TEM imaging (Figure 4.5c-d) reveals that the graphene in 3D-NG is on the order of 10-100 nm thick with an average lattice spacing of 3.47 Å between planes of graphene, with an SAED pattern (Figure 4.5 h) indicating a crystalline structure. The low lithium diffusion length combined with the relatively large lattice spacing in comparison to the theoretical spacing distance of 3.35 Å endows the material with facile lithiation kinetics. As seen by the elemental mapping of the HAADF-STEM image of 3D-NG (Figure 4.5e), the graphene consists of carbon and nitrogen as a result of the nitrogen-containing carbon precursor used for the CVD process. The nitrogen doping improves the interaction between the surface of the graphene and the electrolyte, and provides lithiophilic surface moieties, further improving lithiation kinetics. As seen in the digital photo of 3D-NG (Figure 4.5i), the resulting material is freestanding, thereby circumventing the need for slurry preparation and the use of copper current collectors, which reduces the need for electrochemically-inactive copper in batteries, thereby increasing the energy density of the battery.

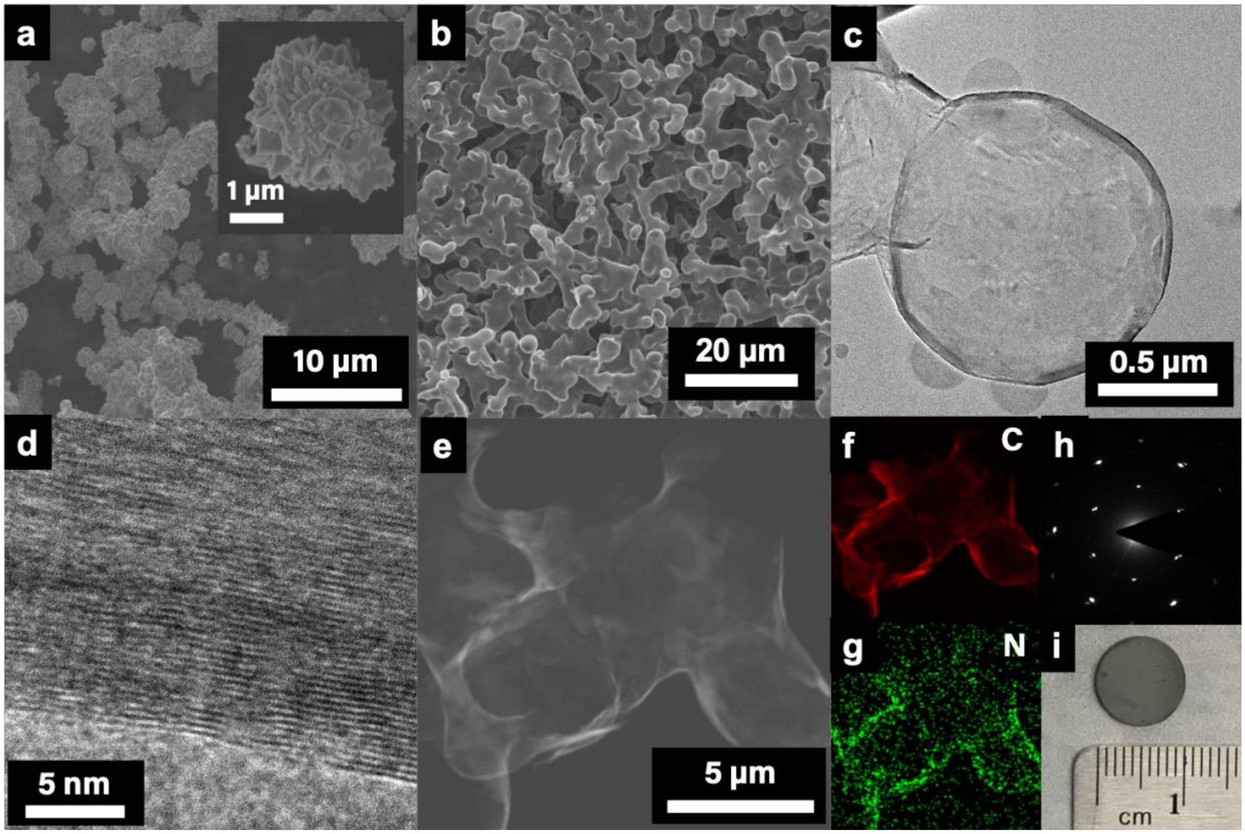

**Figure 4.5** Morphological characterization of 3D-NG. SEM images of a) precursor nickel particles and b) 3D-NG; c-d) TEM imaging of 3D-NG at various magnifications; e) HAADF-STEM imaging of 3D-NG with corresponding element mapping for f) C and g) N; h) SAED pattern of 3D-NG; i) digital photograph of an as-synthesized 3D-NG pellet.

*Structural Characterization*

Structural characterization of 3D-NG is presented in Figure 4.6. The XRD spectrum (Figure 4.6a) of 3D-NG corresponds to graphite with broader peaks than pure graphite, indicating a wider interplanar spacing than pure graphite, consistent with TEM imaging. Raman spectroscopy (Figure 4.6b) reveals a D/G ratio of 0.48, indicating high quality graphene. Nitrogen adsorption/desorption isotherms of 3D-NG (Figure 4.6c) correspond to a surface area of 54.5 $m_2$/g.

For reference, the theoretical specific surface area of pure graphene is 2,630 m$_2$/g. As previously mentioned, specific surface area influences the lithiation kinetics and the ICE, where a large surface area provides more pathways for lithium entry into the material, facilitating quicker charging and discharging at the expense of a lower expected ICE.

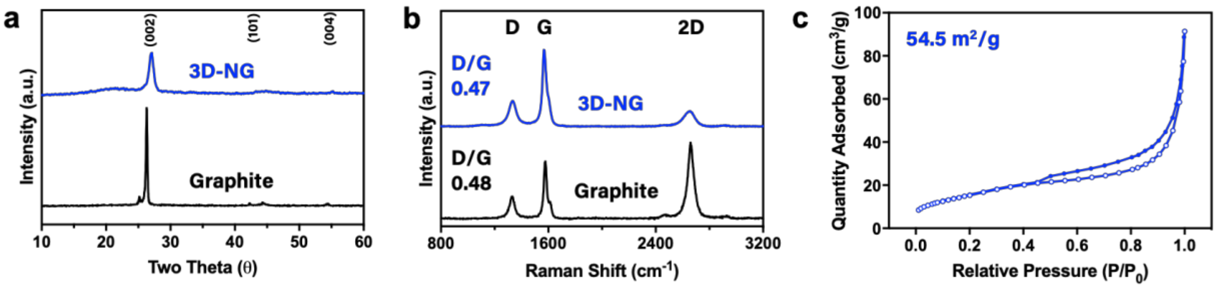

**Figure 4.6** Structural characterization of 3D-NG. a) XRD spectra of 3D-NG and graphite, b) Raman spectra of 3D-NG and graphite, and c) N$_2$ adsorption/desorption isotherms of 3D-NG.

*Electrochemical Performance and Characterization*

Electrochemical performance and characterization of 3D-NG is displayed in Figure 4.7. At a high rate of 1 C, 3D-NG displays a gradual activation process and reaches a high capacity of 285 mAh/g with extremely stable cycling, displaying minimal capacity decay even after 2,000 cycles and minimal increase in charge transfer resistance, as evidenced by EIS (Figure 4.7b). In comparison to graphite, 3D-NG achieves a higher capacity and lower polarization (Figure 4.7c). EIS measurements of 3D-NG and graphite before cycling (Figure 4.7d) reveal a lower charge transfer resistance for 3D-NG, which can be explained by improved electrode-electrolyte interactions of the N-doped graphene, leading to improved lithium transport kinetics. Rate performance of 3D-NG and graphite (Figure 4.7e) was assessed using charge/discharge rates of 0.1, 0.2, 0.5, 1, 2, and 5 C, in which 3D-NG displays capacities of 271, 271, 234, 179, 121, and 65 mAh/g, respectively, whereas graphite displays capacities of 327, 288, 214, 113, 29, and 9 mAh/g, respectively. Although graphite has a higher maximum capacity, 3D-NG utilizes a higher fraction of its maximum capacity at all rates (Figure 4.7f) and surpasses graphite in specific capacity at rates exceeding 0.5 C. At a mass loading near commercial levels (10 mg/cm$_2$), 3D-NG reached a capacity of 1.4 mAh/cm$_2$ at 1 C, whereas graphite had negligible capacity at the same rate, further demonstrating the improved rate performance of 3D-NG (Figure 4.7g).

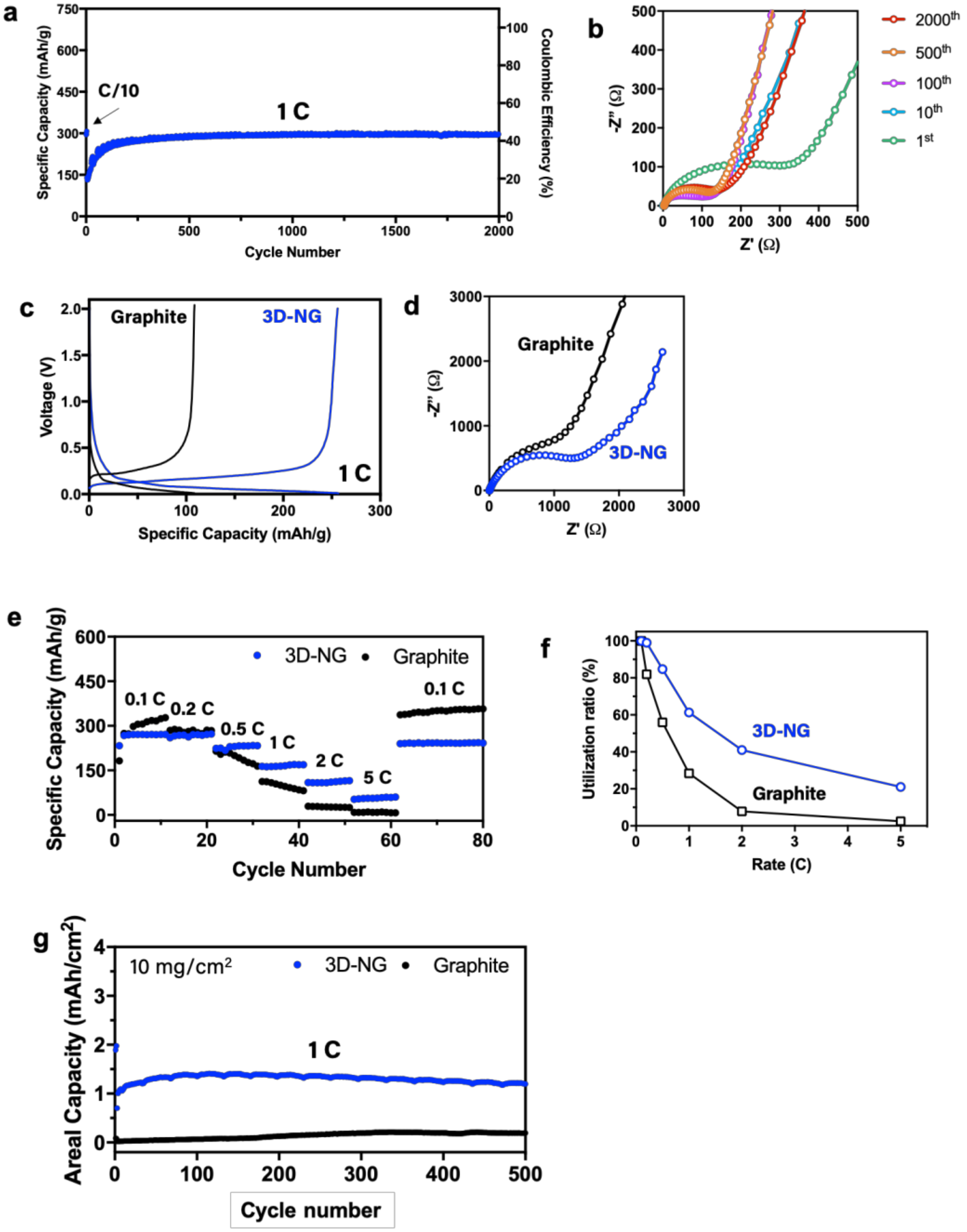

**Figure 4.7** Electrochemical characterization and performance of 3D-NG. a) cycling performance of 3D-NG at a mass loading of 2 mg/cm2 and a rate of 1 C; b) Nyquist plots of 3D-NG before cycling and after the 1st, 10th, 100th, 500th, and 2000th cycles at a rate of 1 C; c) voltage profiles of 3D-NG and graphite using a rate of 1 C; d) Nyquist plots of 3D-NG and graphite before cycling; e) rate performance of 3D-NG and graphite at various C-rates; f) utilization of the 3D-NG and

graphite at various C-rates with respect to the maximum capacity provided by the material; g) cycling performance of 3D-NG and graphite at a mass loading of 10 mg/cm$^2$ and a rate of 1 C.

## 4.7 Conclusions and Significance

The development of next-generation anode materials for lithium-ion batteries generally requires three important characteristics: 1) high energy density; 2) high power density/fast charging capabilities; 3) low cost and scalability. The design and synthesis process for 3D-NG addresses these needs as follows:

### *High energy density*

Most efforts toward the development of lithium-ion batteries with high energy density are focused on developing anode materials with higher specific capacity such as silicon or lithium metal. However, another viable route for increasing the energy density of lithium-ion batteries is by reducing the amount of electrochemically inactive components of the battery on the electrode, cell, or pack levels. Because of the freestanding design, copper current collectors are not necessary, potentially increasing the mass and volume fractions of the electrochemically active components of the cell and thereby increasing the energy density and specific energy of the entire lithium-ion battery.

### *Fast Charging*

One critical aspect for the development of commercially-viable lithium ion batteries for electric vehicles is charging time. Because of the improved electrical conductivity and lithiation kinetics afforded by the design, 3D-NG reaches much higher specific capacity than pure graphite, specifically at high rates, making it the superior material for applications requiring fast charging.

### *Scalability and Low Cost*

As previously mentioned, the typical method for synthesizing graphite for lithium-ion batteries requires heating at high temperatures for extended periods of time. While this method has proven to be scalable, the energy costs end up dominating the cost of the material itself. The method to synthesize 3D-NG with induction heating-mediated chemical vapor deposition represents a much more energy efficient process. Induction heating is fundamentally more energy efficient than a typical tube furnace due to the non-contact nature of the process. Additionally, the heating/cooling times are on the order of seconds, saving the energy costs required during heating and saving significant amount of time, which enable higher scalability (Figure 4.8). Furthermore, the electrode structure of 3D-NG simplifies the battery manufacture process by removing the need for slurry preparation and the need for copper current collectors, which incur additional costs. Together, these factors increase the scalability of material synthesis while simplifying the battery preparation process, reducing overall costs of the process.

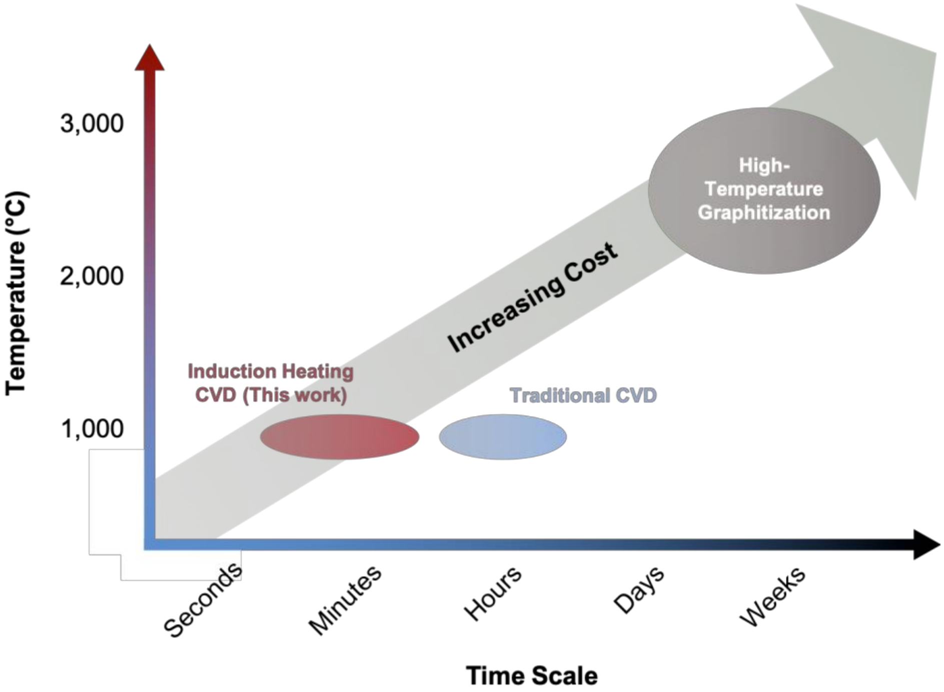

**Figure 4.8** Visualization of temperature and time scales necessary for various synthesis procedures for graphitic carbon anode materials.

## 4.8 Directions for Further Study

*Induction Heating for High-Quality Nanostructured Graphene*

In this project, we have demonstrated a novel method for synthesizing graphene using induction heating as the heating source. While induction heating saves time due to shorter heating/cooling periods required, the ability to reach the target temperature in a short amount of time has other potential benefits. As previously mentioned, there is high interest in developing graphene with specifically designed nanostructure enabling favorable properties for lithium-ion batteries. One key structural consideration is the porosity of the graphene, where a mesoporous structure has been shown to provide higher specific capacity than conventional graphite-like materials. Although transitions metals such as nickel and copper catalyze the formation of graphene, these materials tend to aggregate upon heating due to Ostwald ripening, which eliminates the finer structural features of the template. Because of this phenomenon, it is necessary to use catalysts such as MgO due to its superior thermal stability despite the lower quality of graphene produced. For many applications, it is desired to make graphene with as high quality as possible, so catalysts such as nickel or copper would be preferred over MgO. Through the use of induction heating as the heat source, the effects of sintering can be minimized due to the fast heating process, potentially enabling the use of transition metal catalysts for creating nanostructured graphene with higher quality. Nanostructured graphene with higher quality can lead to improved performance as anode materials in lithium-ion batteries while potentially opening new avenues for materials research in low-density materials with high electrical conductivity and mechanical strength.

### *Three-Dimensional Graphene Current Collectors*

During cycling, electrode particles are subject to volumetric expansion and morphological changes, specifically for high capacity materials such as silicon, potentially leading to electrode pulverization and capacity fading. Previous reports have shown that endowing silicon particles with flexible matrices or coatings improves their cycling stability[38,39]. The ability of flexible materials to conform to surfaces undergoing volumetric expansion and contraction make them ideal surface coatings for anode materials with high specific capacity. In comparison to copper current collectors, 3D-NG is a three-dimensional material that acts as an elastic, electronically conductive highway that provides particles throughout the volume of the electrode with direct contact points with the current collector, improving electronic conductivity and electrode integrity. Furthermore, 3D-NG itself is an anode material, which unlike copper can provide lithium storage and not “dilute” the battery. Finally, the three-dimensional conductive architecture can improve the properties of materials suffering from low intrinsic electrical conductivity such as silicon or essentially all cathode materials. Together, these benefits can potentially enable high-capacity anode materials with improved cycling stability and rate performance.

### *Layer-By-Layer Electrode Design*

As previously mentioned, particles in the electrode rely on the physical connections between adjacent particles in order to maintain electrical contact with the battery and external circuit. Since 3D-NG is a continuous structure as opposed to an ensemble of individual particles, surface modifications to 3D-NG, specifically with electrically insulating materials, will not jeopardize the electronic conductivity of the electrode. Additionally, the freestanding nature of 3D-NG makes it easier to perform additional modifications without compromising the integrity of the electrode, which is much more difficult to do for traditional electrodes held together with polymeric binders.

### *Host for Lithium Metal Anodes*

Lithium metal contains the highest specific capacity and volumetric capacity of any potential anode material for lithium-ion batteries. However, challenges such as the uneven plating of lithium metal and the growth of lithium dendrites makes them unsafe and impractical as anode materials. Previous reports suggest that lithium dendrites grow as a result of high local current densities. As such, the development of three-dimensional hosts can mitigate this issue by providing more surfaces for lithium metal deposition, reducing local current density. With a relatively high specific surface area of 54.5 $m_2$/g, 3D-NG can serve as a host for lithium metal anodes.

Additionally, N-doped graphene reduces the nucleation potential of lithium metal, resulting in more even lithium plating and reduced dendrite growth[40]. Following the design of a previous report[41], gold nanoparticles grown on the surface of the nickel template can be used as nucleation sites to guide the deposition of lithium metal on the interior voids of 3D-NG, protecting the surface of lithium metal from the electrolyte and improving coulombic efficiency.

Although in theory 3D-NG can improve the performance of lithium metal anodes, many believe that lithium metal anodes will only be realized in conjunction with solid-state electrolytes (SSEs) due to the extremely low coulombic efficiencies achieved with liquid electrolytes. Typically, SSEs are constructed in a two-dimensional membrane film that covers the surface of a two-dimensional lithium metal disc. Using this approach, the SSE membrane undergoes dramatic movement to maintain contact with the electrode as lithium metal is plated and stripped. Using 3D-NG as a host, lithium metal can be deposited on the interior surface with SSE residing on the outer surface, circumventing the need for dramatic movement of the SSE to improve electrode integrity.

# 5. Ball-Milled Silicon/PVA/Graphite Composites for Scalable, Low-Cost Anodes for Lithium-Ion Batteries

## 5.1 Introduction

Silicon, with a high specific capacity of 3,579 mAh/g and low cost, has been extensively studied as a potential anode material for high energy density lithium-ion batteries. However, many intrinsic properties of silicon, including low electrical conductivity, low lithium diffusivity, and massive volumetric expansion during lithiation, pose challenges towards the development of commercially-viable silicon anodes. While many intricate silicon anode material designs with exceptional performance have been reported in the literature, widespread adoption of such designs are hindered by prohibitive material fabrication costs and difficulty in scaling such processes. In order to realize commercially-viable silicon anodes, low-cost and scalable material design processes must be used while maintaining the design principles of the aforementioned literature-described designs.

## 5.2 Principles of Silicon Anodes

### *Electrochemical Properties*

Silicon is an alloy anode material for lithium-ion batteries that when fully lithiated has a stoichiometric ratio of 15 to 4 of lithium to silicon, representing a specific capacity of 3,579 mAh/g. During lithiation, silicon and lithium undergo continuous phase transitions (Figure 5.1) with an average electrochemical potential of around 0.4 V vs $Li^+/Li$. This potential is ideal for anode materials since it enables high operating potentials in full cells while maintaining enough separation from the reduction potential of lithium to prevent lithium dendrite formation. As a result of the phase transformations, silicon reverts to amorphous silicon upon delithiation, enabling faster lithium transport kinetics for subsequent cycles.

**Figure 5.1** Crystallographic changes of silicon during lithiation.[42]

Despite the high specific capacity afforded by silicon, its intrinsically low electrical conductivity ($4 \times 10^{-4}$ S/m), low lithium diffusivity ($10^{-13} – 10^{-11}$ $cm^2/s$) and massive volumetric expansion upon lithiation (~ 270%) creates several unwanted side effects that diminish its cycling performance. As a result of the low electrical conductivity and lithium diffusivity, silicon anodes experience a high degree of ohmic and concentration polarization, reducing the specific capacity and energy efficiency of the material. In what is arguably an even larger issue, the massive volumetric expansion creates a dynamic interface between electrode particles and the electrolyte, resulting in repeated formation and fracture of the SEI during cycling that leads to rapid capacity decay and impedance buildup. Additionally, large-scale expansion of the electrode results in pulverization and electrical detachment of silicon particles, contributing to additional capacity decay. In order to produce commercially viable silicon anodes, all of these intrinsic drawbacks must be adequately addressed to enable high capacity and long cycling life.

*Particle Fracture*

During lithiation, the phase transformations occurring on the boundaries of silicon particles leads to anisotropic volume expansion, imposing immense strain on the crystal lattice of silicon particles. Previous in situ TEM observations revealed that silicon particles with crystalline sizes surpassing ~ 150 nm fracture upon lithiation[43,44]. During this violent process, fresh faces of silicon are exposed and subsequently react with the electrolyte to form new SEI while the resulting silicon particle fragments may easily become electrically isolated, leading to rapid capacity decay.

## 5.3 State-of-the-Arts

*Nanosizing*

Nanosizing silicon particles is an effective and widely-used strategy for mitigating issues associated with particle fracture and slow lithiation kinetics. Similar to graphene synthesis, silicon nanoparticle synthesis typically follows two general approaches: top-down and bottom-up. Top-down approaches such as ball milling of micron-sized silicon particles has proven to be an effective method for producing nanoscale silicon with excellent cycling properties[45]. Bottom-up approaches typically use precursors such as silane gas ($SiH_4$) to produce silicon nanoparticles via CVD. As previously stated, CVD processes are difficult to scale due to limited batch sizes and long process times. For both top-down and bottom-up approaches, additional modifications must be made in order to overcome the challenges imposed by the other disadvantages of silicon, including the dynamic interface and low electrical conductivity.

### *Carbon Compositing and Surface Modification*

Compositing silicon with conductive materials is a popular method for overcoming the low electrical conductivity of silicon. Due to its low cost, low density, and wide array of design choices, carbon is typically the material of choice for enabling this performance enhancement. Additionally, protective coatings of carbon or other materials over the surface of silicon particles may reduce reactions between the electrolyte and silicon, decreasing the consumption of electrolyte and lithium and thereby prolonging the cycling life of the electrode.

### *Void Space Accommodation*

Due to the unavoidable volumetric expansion of silicon, protective coatings over the surface of silicon may fracture, thereby enabling parasitic reactions between silicon particles and electrolyte and resulting in electrode pulverization. One novel design for mitigating this issue was through the development of "yolk-shell" structures in which silicon nanoparticles were imbedded in a hollow carbon shell containing void space to accommodates volumetric expansion without pulverization. Such a strategy has been employed by many researchers working on alloy anode materials for lithium-ion batteries[38,46–49]. Despite this clever design approach, such architectures are complex, leading to excessively high costs and bringing scalability into question. Furthermore, hollow structures typically have low mechanical strength, easily resulting to particle fracture. Simpler, more robust methods are desired for practical, large-scale production of silicon anodes.

### *Electrolyte Additives*

Capacity decay due to repeated formation and fracture of the SEI is a common phenomenon inhibiting the commercial viability of silicon anode materials. To address this issue, it is relatively common to use electrolyte additives such as fluoroethylene carbonate (FEC) with silicon anodes. Previous reports indicate FEC creates a more robust SEI due to its tendency to form polymeric SEI components that can conform to the dynamic interface of silicon particles during cycling, reducing SEI fracture[50]. As a result, tremendous improvements in cycling life are observed when using FEC or similar additives.

### *Silicon Monoxide*

Silicon monoxide, with a chemical formula of $SiO_x$ ($0 < x < 2$), has displayed promise as a silicon-based anode material with exceptional cycling stability. Upon the first lithiation, silicon monoxide undergoes a series of transformations eventually leading to the formation of nanosized silicon particles within a matrix of lithium oxide and lithium silicates[51,52]. This matrix serves as a protective coating that buffers the volumetric expansion of silicon during cycling, leading to tremendous cycling performance. Despite this attractive feature, silicon monoxide contains many glaring disadvantages, such as an extremely low ICE (typically below 50%) due to irreversible reactions between lithium and oxygen from silicon monoxide during the first lithiation. Furthermore, silicon monoxide is much less conductive than pure silicon, which itself already suffers from low intrinsic conductivity, leading to poor rate performance. On top of these disadvantages, silicon monoxide is expensive to produce and questionable in scalability, further limiting its commercial viability. For these reasons, silicon monoxide thus far has only been utilized as an anode additive to provide modest boosts in specific capacity.

*Commercial Silicon Anodes*

Currently, silicon-based materials account for just 2% of the market share of anode materials for lithium-ion batteries[22]. Although many publications have described novel methods for silicon anode particle preparation, there is not much public information on commercial processes for silicon particle preparation, other than the fact that only a small amount of silicon (5 – 20% by mass) is typically incorporated into the anode[53]. Two practically suitable methods for the production of silicon-based anode materials is presented in Figure 5.2. First, silicon nanoparticles are produced via plasma phase gas synthesis[54], while $SiO_x$ particles are obtained by reduction of SiO or $SiO_2$ via milling or gas phase reactions[51,55]. Afterwards, the silicon particles are embedded in a carbon matrix either by mixing with graphite or carbon precursors followed by additional carbonization and milling. Finally, carbon coating and other processes are used to optimize the specific surface area to achieve the desired performance[32].

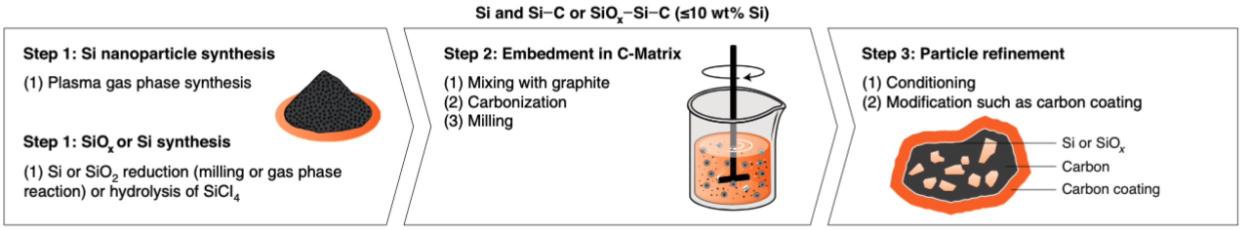

**Figure 5.2** Production process for silicon-based anode materials.[14]

With graphite presently unable to satisfy the high energy density requirements of lithium-ion batteries for electric vehicles, silicon-based anode materials have already been incorporated in anodes for electric vehicles, including in the Tesla model X and Tesla model 3. Although it is likely that only a small mass fraction of silicon is incorporated, the extremely high specific capacity of silicon compared to the commercial standard graphite can cause significant increases in capacity. Whereas most electric vehicles do not have a driving range over 500 km, the Tesla model 3, which contains silicon in the anode, has a maximum range of 630 km (Table 2.1).

## 5.4 Design and Process Overview

Considering how anodes make up a much smaller contribution to material costs of batteries in comparison to other parts, most notably the cathode, it is impractical to improve the performance of the anode while incurring excessive costs. In order to make use of the insights provided by the literature on high-performance silicon anodes, it is therefore necessary to pursue alternative strategies exclusively using low-cost precursors, scalable operations, and simple fabrication processes.

Following this design philosophy, we herein describe a scalable, 1-step ball milling process using low-cost precursors to produce silicon composite anodes with exceptional cycling stability. Ball milling is an industrial process already used for large-scale production of many materials requiring small particle size or high surface area such as coal or black powder.[56] As previously mentioned, high-energy ball milling of low-cost bulk silicon can produce nanosized silicon particles with cycling properties comparable to those of expensive silicon nanoparticles synthesized via chemical vapor deposition (CVD) of silane gas. Following previous work revealing the remarkable improvement in cycling performance of ball-milled silicon upon the addition of polyvinyl alcohol (PVA) to the milling process, we further improve its cycling performance through the addition of graphite to the ball milling process, as depicted in Figure 5.3.

Previous work demonstrated that during the milling process, the hydroxyl groups of PVA reacts with the high-energy dangling bonds of silicon exposed as a result of mechanical fracture of silicon particles, producing silicon particles wrapped in a robust polymer coating that buffers the volumetric expansion of the silicon particles, leading to improved cycling life. The addition of graphite to the ball milling mixture causes the graphite to exfoliate into multilayer graphene which then coats the surface of silicon particles. Graphite, the commercial anode material of choice for many LIBs, is notoriously stable due to its stable interface with the electrolyte, minimizing the fracture and reformation of the SEI. By virtue of the multilayer graphene coating, the silicon composite anode materials are endowed with high stability and improved conductivity, resulting in high energy density and long cycling life.

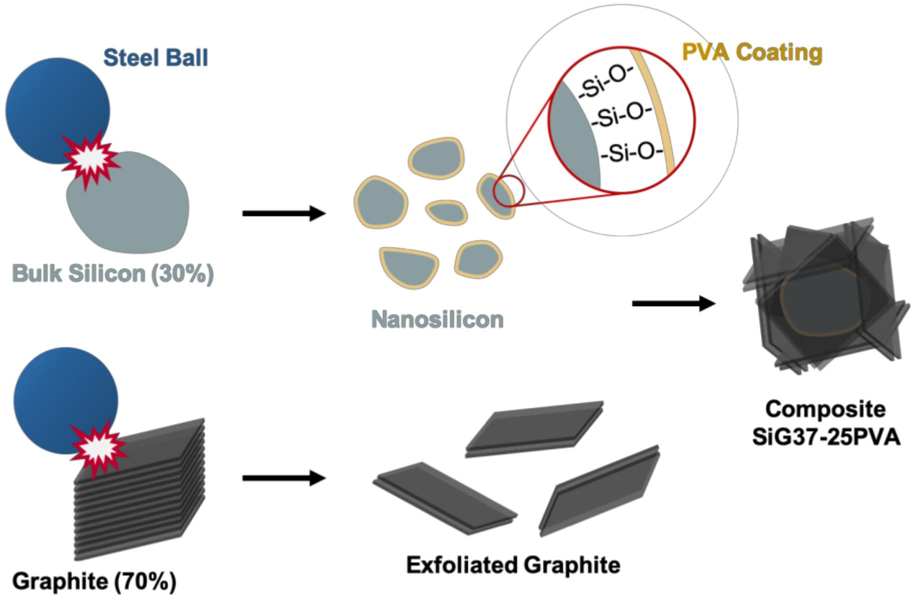

**Figure 5.3** Schematic illustration of the ball milling process.

## 5.5 Methods

*Preparation of silicon/PVA/graphite composites:* Bulk silicon, PVA, and graphite were milled in a high-energy ball miller (Retsch) at a ratio of 3:7 silicon:graphite with various amounts of PVA used as an additive. The milling jars were sealed in an argon atmosphere and milled with stainless-steel balls and jars at a ball:material ratio of 12:1 for a total of 10 h at 1,000 rpm using 10 min on/10 min off intervals. Using PVA as a 25 mass% additive, the resulting composite is denoted as SiG37-25PVA.

*Materials Characterization:* XRD spectra were obtained with a Rigaku powder X-ray diffractometer (XRD) using Kα radiation (λ = 1.54 Å). Transmission electron microscopy (TEM) images were obtained with Titan S/TEM scanning transmission electron microscope (FEI). Scanning electron microscopy (SEM) images were taken with a Nova 230 Nano SEM. Raman spectra were obtained with a Renishaw 2000 System with a He/Ne laser at a wavelength of 633 nm. Thermogravimetric analysis (TGA) was performed in air using a ramping rate of 10 $_{o}$C min$_{-1}$. Gas sorption measurements were conducted using a Micromeritics ASAP 2020 system at 77 K. Prior to gas adsorption/desorption measurement, all power was degassed at 120 °C for 12 h. For X-ray photoelectron spectroscopy (XPS) studies, AXIS Ultra DLD was used for analysis. All the spectra were fitted to Gaussian–Lorentzian functions and a linear-type background using CasaXPS software. The binding energy values were all calibrated using C 1s peak at 284.5 eV.

*Coin Cell Assembly:* Electrodes were prepared by preparing an electrode slurry containing active material/acetylene black/poly(acrylic acid) as a 7/1.5/1.5 ratio in NMP solvent. After stirring overnight, the slurry was casted onto a Cu foil current collector using a doctor blade and dried in a vacuum oven at 90 °C. The resulting active material mass loading was approximately 1.0 mg/cm$_2$ unless otherwise noted. Half-cells were assembled 2032-type coin cells using Li foil as the counter/reference electrode, 1 M $LiPF_6$ in a mixture of ethylene carbonate (EC)/dietyl carbonate (DEC) containing 5 vol% fluoroethylene carbonate (FEC) as the electrolyte, and porous polypropylene separators.

*Electrochemical Characterization:* Cyclic voltammetry (CV) measurements were conducted using a Solartron 1860/1287 electrochemical station with a scan rate of 0.05 mW/s from the open circuit voltage (OCV, 2 – 3 V vs. Li/Li$_+$) to 0 V and back to 2 V. Electrochemical impedance spectroscopy (EIS) measurements were taken using an amplitude of 100 mV and frequencies ranging from 100 kHz to 10 mHz. Cycling performance was conducted with a LAND battery testing system (China). Specific capacities were calculated based on the total mass of the active material.

## 5.6 Results and Discussion

### *Materials characterization*

Morphological characterizations of SiG37-25PVA and its precursors are displayed in Figure 5.4. While the precursor materials (Figure 5.4a-b) had particle size on the order of tens of microns, the resulting composite (Figure 5.4c) had particle sizes on the order of 1 µm. As seen in the TEM image of SiG37-25PVA (Figure 5.4d), individual silicon particles can be seen clustered within a matrix of exfoliated graphite sheets. High-resolution TEM (Figure 5.4e-f) imaging reveals a material with a lattice spacing of 0.31 nm, corresponding to silicon, coated with a mixture of an amorphous layer and a multilayer material resembling graphene, suggesting the silicon particles are encapsulated in the graphite, consistent with SAED imaging (Figure 5.4g). As revealed in previous reports, the coating of exfoliated graphite on the nanoscale silicon particles may protect the silicon particles from the electrolyte and enhance the electrical conductivity of the composite, improving its cycling performance.

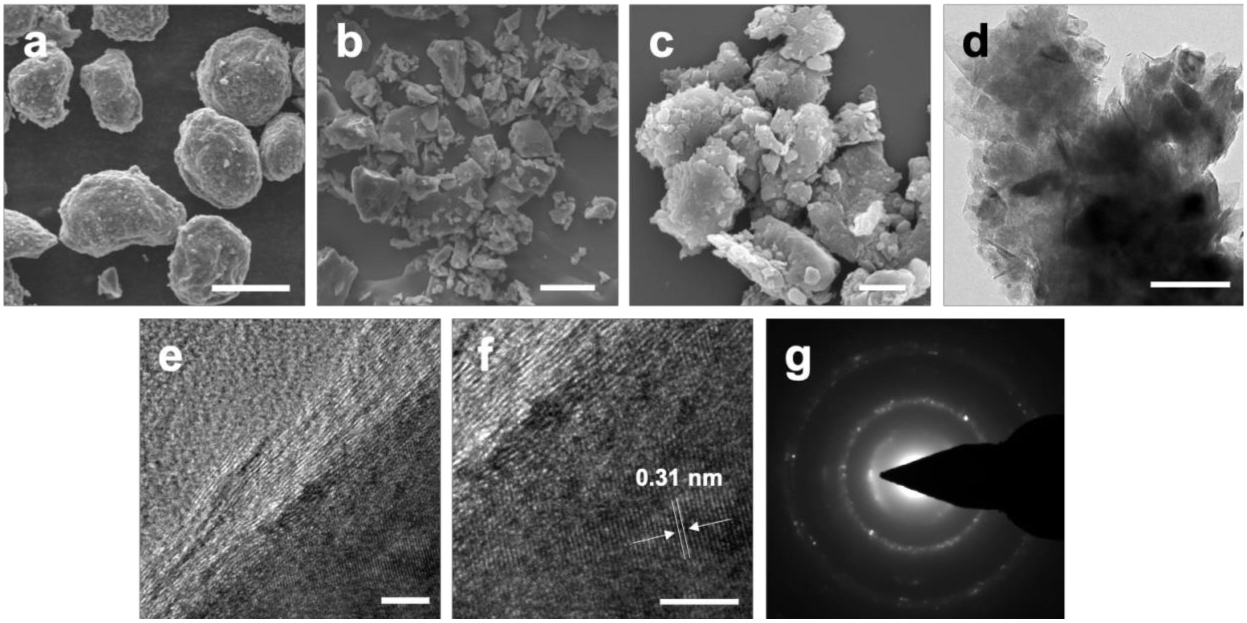

**Figure 5.4** Structure and morphology of SiG37-25PVA. SEM images of a) graphite particles; b) silicon particles; c) SiG37-25PVA particles. d-f) TEM SiG37-25 PVA of particles. g) SAED image of SiG37-25PVA particles. Scale bars: a 20 µm; b 10 µm; c 2 µm; d 0.5 µm; e 5 nm; f 5 nm.

*Structural and Chemical Characterization*

Structural and chemical characterization of SiG37-25PVA is displayed in Figure 5.5. As revealed by XRD spectroscopy (Figure 5.5a), the SiG37-25PVA composite displays much broader peaks of silicon and graphite compared to the precursor materials, suggesting a higher density of crystalline defects common among materials with higher specific surface area and smaller particle size. The higher defect density in the material facilitates the lithiation of the material and makes the volumetric expansion of the silicon more even, improving the rate performance and cycling stability of the material. Additionally, the reduced particle size of the silicon particles can help prevent fracture of silicon crystallites caused by buildup of stress during the lithiation process, reducing pulverization of the electrode. Raman spectra of SiG37-25PVA and the graphite precursor (Figure 5.5b) reveals a higher D/G ratio for SiG37-25PVA compared to the graphite precursor, indicating a higher density of defects in the graphene of SiG37-25PVA. Defects of graphite have previously been reported to react with hydroxyl-containing substances such as water, which may assist in the formation of covalent bonds between PVA and graphite, further improving the structural integrity of the material. Additionally, defects have been shown to improve lithiation kinetics by providing additional pathways for lithium transport[57], improving rate performance. TGA results (Figure 5.5c) reveal SiG37-25PVA retains only 31% of its original mass in air at 600 °C. Considering how silicon accounts for 24% of the original mass and PVA and graphite completely decomposes at high temperature, the additional mass retention is attributed to the formation of a thermally stable Si-O-C layer on the surface of the silicon particles where the C and O moieties are from the PVA, as indicated from previous results. XPS results (Figure 5.5d) reveals that after milling, no silicon is detected for SiG37-25PVA. Considering that XPS has a surface penetration of around 5 nm, the lack of a silicon signal indicates the silicon particles are likely completely covered in the graphite layers. BET measurements (Figure 5.5e) reveal that the specific surface areas of SiG37-25PVA and SiG37 without PVA are 71.8 $m^2$/g and 229 $m^2$/g, respectively. This reveals the role of PVA in reducing the specific surface area of the material, acting as a material that “glues” the surfaces of the material together to promote structural integrity.

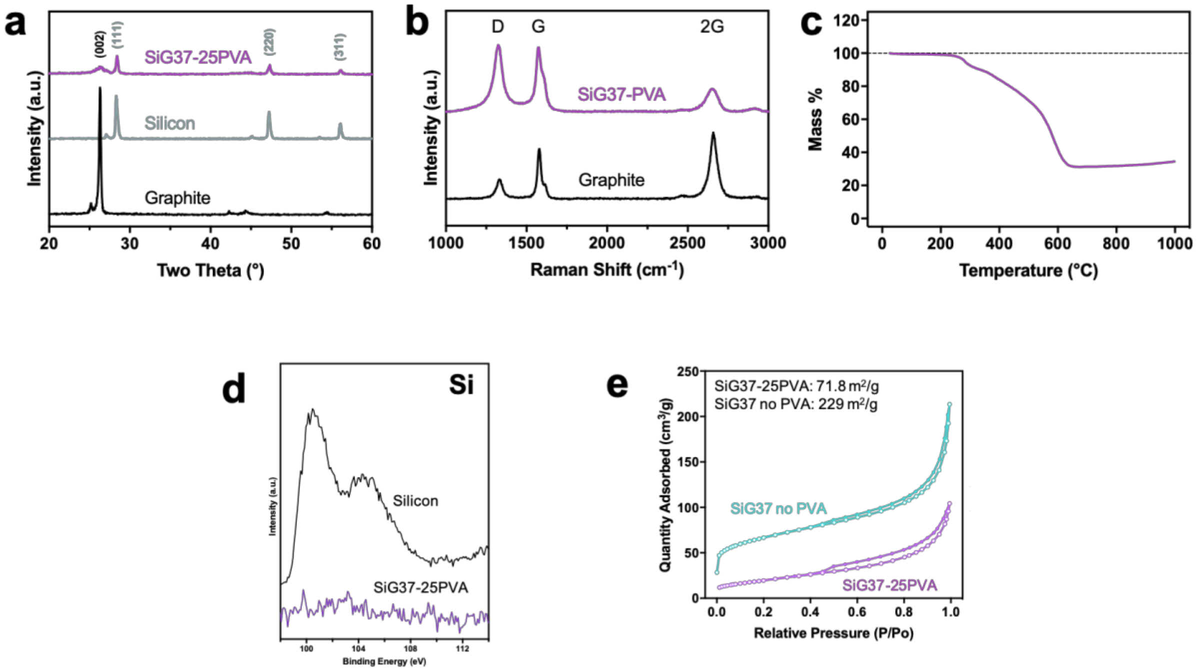

**Figure 5.5** Structural characterization of SiG37-25PVA. a) XRD spectra of SiG37-25PVA, bulk Si, and graphite; b) Raman spectra of SiG37-25PVA, graphite; c) TGA of SiG37-25PVA performed in air at a ramp rate of 10 °C/min; d) Si 2p XPS spectra of SiG37-25PVA and bulk silicon precursor; e) $N_2$ adsorption/desorption isotherms for SiG37-25PVA and SiG37 (no PVA) used to determine specific surface area.

*Electrochemical Performance Characterization*

Electrochemical performance and characterization of SiG37-25PVA is displayed in Figure 5.6. As seen in Figure 5.6a, SiG37-25PVA displays an ICE of 70% and a working capacity of 681 mAh/g at 0.5 A/g that lasts 150 cycles without dropping below 80% of its original capacity, indicating remarkable stability when considering the simplicity and low cost of the design. Without PVA, the composite quickly fades in capacity, indicating the crucial role of PVA in cycling performance. Cyclic voltammetry (CV) measurements of SiG37-25PVA (Figure 5.6b) reveals lithiation peaks at 0.18 V and delithiation peaks at 0.16, 0.35, and 0.52 V. The delithiation peak at

0.16 V is characteristic of graphite, indicating that the graphite used retains its electrochemical storage properties, while the peaks at 0.35 and 0.52 V are indicative of silicon. Additionally, the first cycle reveals a slight increase in current in the range of 0.25 – 1 V that is not present on subsequent cycles, consistent with the formation of the SEI on the first cycle. The voltage profiles of SiG37-25PVA (Figure 5.6c) reveals slight overpotential during the first cycle that becomes less dramatic and more stable on subsequent cycles, suggesting the formation of robust lithiation channels after activation on the first cycle. EIS measurements throughout cycling (Figure 5.7d) reveal a drop in charge transfer resistance after the first cycle, indicating the formation of the SEI which aids in the charge-transfer process from the electrolyte to the electrode materials. Over the course of the next 100 cycles, the charge transfer resistance remains relatively stable with a slight increase over this period, suggesting stable cycling. Rate performance of SiG37-25 and graphite (Figure 5.6e) was assessed using current densities of 0.3, 1, 2, and 3 A/g, in which SiG37-25PVA attained specific capacities of 786, 641, 389, and 247 mAh/g, respectively, whereas graphite attained specific capacities of 282, 109, 98, and 47 mAh/g, respectively. At all rates, higher utilization of the maximum specific capacity was achieved by SiG37-25PVA, likely due to the improved lithiation kinetics afforded by the high defect density of the silicon and graphite in SiG37-25PVA. To further assess its commercial viability, the composite material was prepared using silicon/graphite ratios of 3:7 and 5:5, denoted as SiG37-25PVA and SiG55-25PVA, respectively, and the resulting composites were blended with pure graphite at a 50/50 mass ratio. When using a mass loading of 5.5 mg/cm$_2$ and a rate of 100 mA/g, the SiG55-25PVA/Graphite and SiG37-25PVA/Graphite mixtures attain areal capacities of over 4 mAh/cm$_2$ and 3 mAh/cm$_2$, respectively, compared to pure graphite at around 1 mAh/cm$_2$ (Figure 5.6f). Under these cycling conditions, the SiG55-25PVA/Graphite and SiG37-25PVA/Graphite electrodes retain over 80% and 90% of their maximum capacity after 100 cycles, respectively.

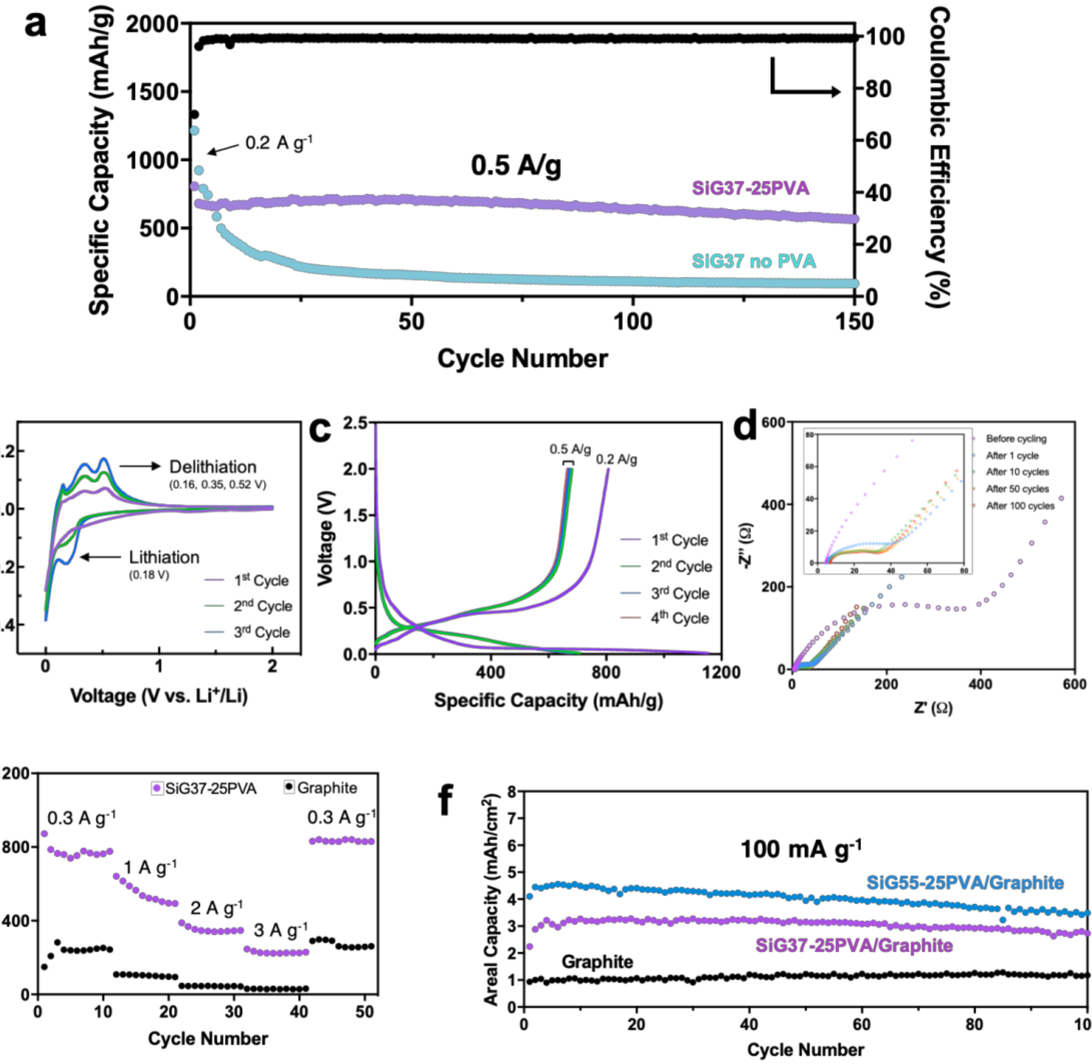

**Figure 5.6** Electrochemical performance and characterization of SiG37-25PVA. a) Nominal cycling performance of SiG37-25PVA and SiG37 (no PVA) using a current density of 0.2 A/g on the first cycle and 0.5 A/g on subsequent cycles. Coulombic efficiency corresponds to SiG37-25PVA. The mass loading for both electrodes was approximately 1.0 mg/cm2; b) CV of SiG37-25PVA starting from the open circuit voltage (approx. 2 V vs Li/Li+) and cycling between 0 and 2

V at a rate of 0.05 mV/s; c) Voltage profiles of SiG37-25PVA for the first four cycles where a current of 0.2 A/g is used for the first cycle and a current of 0.5 A/g is used for subsequent cycles; d) Nyquist plots of SiG37-25PVA before cycling, and after 1, 10, 50 and 100 cycles; e) rate performance of SiG37-25PVA and graphite. The mass loading for both electrodes was approximately 1.0 mg/cm$^2$; f) cycling performance of SiG55-25PVA and SiG37-25 PVA when used in a 50%/50% mixture with graphite, and pure graphite under high loading (5.5 mg/cm$^2$) at a current density of 100 mA/g.

## 5.7 Conclusions and Significance

Silicon is a highly sought anode material owing to its exceptionally high theoretical specific capacity and low cost. While many companies have already managed to commercialize silicon anode materials, widespread adoption is hindered largely by cost and scalability. This work provides a 1-step procedure for silicon/graphite composite anodes with exceptional stability and rate performance that is both scalable and uses only low-cost precursors. Although SiG37-25PVA possesses a modest specific capacity (681 mAh/g at 0.5 A/g), it attains nearly twice the specific capacity of graphite, the current industry standard anode material. Previous reports suggested that ball milling likely costs around $250 to mill 100 kg of material[45]. Although further improvements to the design is likely necessary in order for the performance to be commercially viable, the extremely low cost opens up the possibility of further modification of the composite without compromising price and scalability.

## 5.8 Directions for Further Study

### *Spray Drying of Composite*

This project reveals a 1-step scalable and low-cost route for silicon/PVA/graphite composite anodes with excellent cycling stability. Although the high specific capacity of the material paves the way for lithium-ion batteries with high specific energy, nanosized materials typically possess low tap density, resulting in a low volumetric capacity and low energy density. This disadvantage can be resolved through the use of spray drying of SiG37-25PVA. Spray drying is another industrial process used for large-scale processes at low cost, specifically used in applications where a high tap density is desired such as in the processing of food products. Spray drying takes an aqueous precursor solution/suspension and produces microparticles consisting of the solution/suspension components possessing a much higher tap density. Spray drying the SiG37-25PVA composite follows the philosophy of low cost and scalability and enable the material to achieve a much higher volumetric capacity. Although it is likely that further modifications may be necessary to improve the cycling performance of the spray-dried particles, many reports have already demonstrated the versatility of the spray drying process, which can be used to create particles of various morphology, size, and porosity without the need for any additional equipment.

# 6. A Powder Metallurgic Approach Towards High-Performance Lithium Metal Anodes

## 6.1 Introduction

As the metal possessing the lowest reduction potential (-3.04 vs the standard hydrogen electrode) and density (0.53 g/cm$^3$), lithium (Li) metal possesses the highest possible specific and volumetric capacity (3,860 mAh/g and 2,047 mAh/cm$^3$, respectively) and lowest working potential among all anode materials for lithium-based batteries. By virtue of these properties, lithium metal anodes enable the highest possible specific energy, energy density, and operating voltage on the cell level. Despite these attractive qualities, lithium metal poses many cost, performance, and safety concerns, rendering them far from achieving practical application.

## 6.2 Principles of Lithium Metal Anodes

*Volumetric Expansion*

As a “hostless” anode material, lithium metal is plated and stripped direct to/from its metallic form on various surfaces of the electrode. Under this consideration, the volumetric expansion of the material is considered infinite, requiring specific capacity to therefore be defined in terms of capacity per unit mass of lithium, rather than per unit mass of host. In comparison to silicon, lithium metal therefore possesses a much more dynamic interface between electrode and electrolyte, exacerbating issues related to repeated formation/fracture of the SEI that leads to rapid capacity fading. As a result of the limitless volumetric expansion and contraction of lithium metal, the SEI may undergo significant migration throughout the course of cycling. In addition to the risk of SEI fracture, uneven formation of the SEI may lead to uneven plating of lithium, potentially leading to long-term structural changes in the electrode such as the formation of pores, leading to capacity fading.

### *Lithium Dendrite Growth*

Lithium dendrite growth arguably the largest issue facing lithium metal anodes in terms of performance and safety. Lithium itself is a metallic and ductile material that unlike host particles such as graphite and silicon is prepared as a film with relatively high specific surface area. As a result, cycling under moderate rates results in high local current densities on the electrode surface. When cycled at high rates for sufficient time, the localized concentration of lithium ions in regions close to the surface of the anode will drop, eventually reaching the point where the concentration of lithium ions in the electrolyte near the surface of the anode reaches zero. When this occurs, the negative charge of the anions in solution draws lithium ions from further away into the electrolyte towards the surface of the electrode in a self-propagating fashion, resulting in accelerated plating of lithium ions that result in the growth of lithium metal dendrites protruding from the surface of the electrode[58,59]. The growth of lithium dendrites leads to several unwanted effects, such as the formation of additional SEI that consumes lithium, the formation of "dead" lithium metal nodes from uneven stripping/plating, and the possibility of forming a short circuit in the battery, leading to cell failure and thermal runaway, posing serious safety concerns.

### *Lithium nucleation*

The nucleation of lithium metal is an important phenomenon with many ramifications on the performance of lithium metal anodes. Larger barriers to lithium metal nucleation may lead to fewer nucleation sites and therefore fewer sites for lithium metal deposition, resulting in increased local current densities in the regions of the nucleated lithium. A study on the lithium nucleation behavior on various materials revealed that metals with alloy phases with lithium near room temperature tend to result in lower overpotential for lithium metal nucleation (Figure 6.1). Such materials are therefore advantageous for attenuating lithium dendrite growth, improving cycling performance and safety.

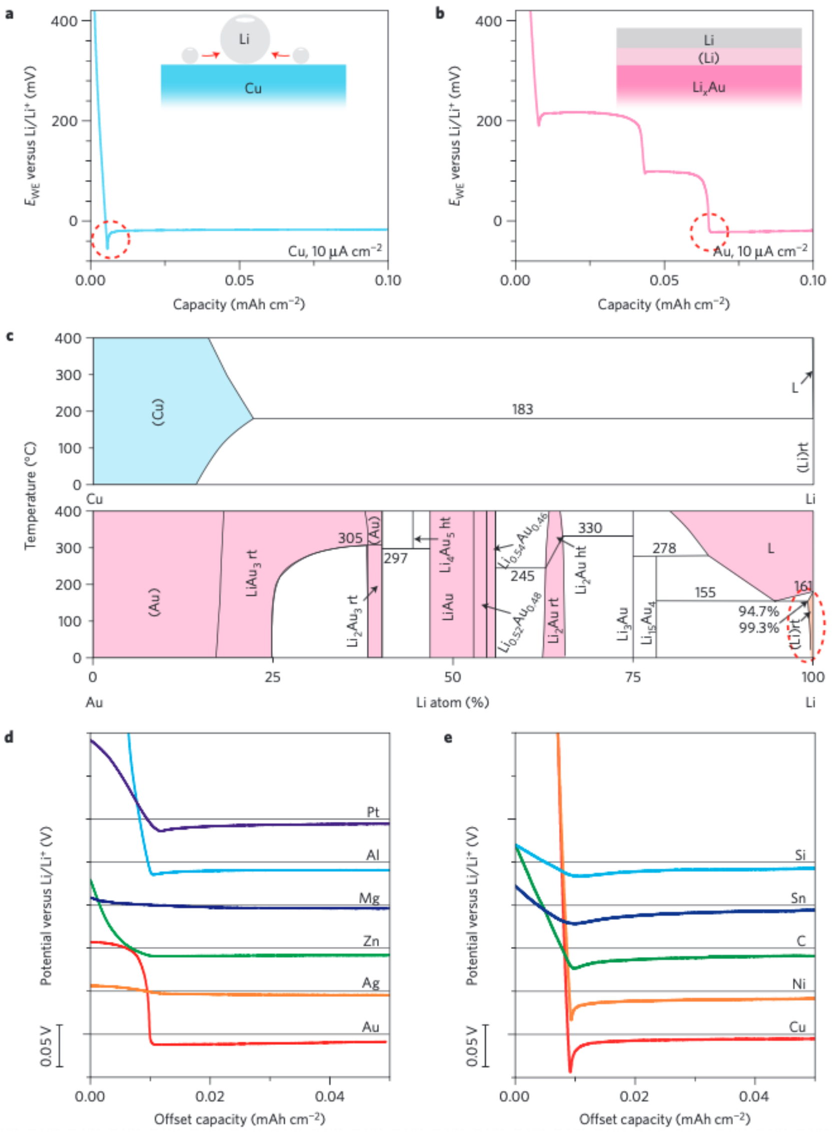

**Figure 6.1** Overpotential during Li deposition on various substrates. a) Voltage profiles of galvanostatic Li deposition on a copper substrate at 10 µA/cm2; b) Voltage profiles of galvanostatic Li deposition on a gold substrate at 10 µA/cm2; The inset shows a schematic of how the solid solution buffer layer of Au dissolved in Li reduces the nucleation energy; c) Phase diagrams of Li with Cu (up) and Au (bottom); d) Voltage profiles of various materials with some solubility in Li during Li deposition at a current density of 10 µA/cm2; e) Shifted voltage profiles of various materials with negligible solubility in Li during Li deposition at a current density of 10 µA/cm2.[60]

## 6.3 State-of-the-Arts

*Commercial Preparation of Lithium Metal*

A typical process for the preparation of lithium metal foil is illustrated in Figure 6.2. Lithium-containing brines are first concentrated via evaporation and converted to LiCl. After purification, electrolysis is used to convert LiCl it to Li metal, followed by distillation to remove impurities such as Na. Finally, the Li metal is extruded into the desired shape using methods such as extrusion/rolling, followed by passivation of the surface[61].

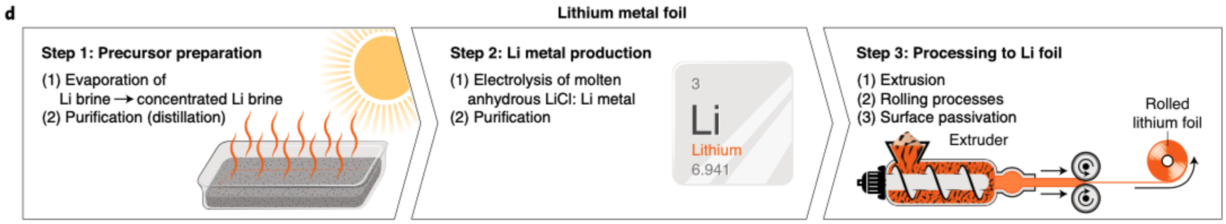

**Figure 6.2** Preparation of Li metal foil.[14]

The price of lithium metal ingots is roughly 50-130 $/kg, which may be as high as $1,000/kg for much thinner foils (less than 100 µm)[62,63]. Considering LIB materials are typically much less than $100/kg, this represents an enormous barrier for widespread adoption of lithium metal anodes. Although the exceptional performance of lithium metal anodes enables niche applications, cheaper methods for lithium metal anode production will be necessary in order to gain significant market penetration.

*Electrolyte Additives*

Many electrolyte additives have been explored in order to improve the cycling properties of lithium metal anodes. Inert cations such as $Cs^+$ and $Rb^+$ added in small amounts were found to inhibit dendrite growth by creating a "self-healing electrostatic shield" around potential lithium dendrite formation locations[64]. Following the Nernst equation, the reduction potential of these cations falls below that of lithium at low concentrations, which prevents deposition of these metals on the surface of lithium. Under conditions in which the local concentration of lithium ions reaches zero near the surface of the electrode, these cations will be attracted to this location, creating an accumulation of positive charge that repels lithium ions. In addition to FEC, lithium nitrate and lithium polysulfides were found to form an SEI that significantly reduces electrolyte decomposition, leading to improved cycling performance[65]. Although these methods improve the coulombic efficiency and cycling stability of lithium metal anodes, additional measures are necessary for adequate cycling performance.

### *Interfacial Engineering*

Considering how all the relevant phenomena influencing the performance and safety of lithium metal anodes occur on the interface of lithium metal and electrolyte, it comes as no surprise that engineering the interface is a popular strategy for improving cycling performance. Theoretical calculations have shown that an interface with a Young's modulus greater than 6 GPa is sufficient for preventing dendrite growth[66]. An interface composed of interconnected hollow nanospheres with a Young's modulus of 200 GPa was found to suppress lithium dendrite growth and enable more uniform lithium deposition on the electrode surface. In addition to inhibiting dendrite growth, other designs for lithium metal interfaces were focused on the formation of a robust passivation layer to prevent excessive SEI formation[67]. Hybrid silicate coatings grown via chemical vapor deposition was found to create a rigid yet flexible SEI layer capable of conforming to the surface of lithium metal during the dynamic cycling process, significantly improving the lifetime of lithium metal anodes[68]. Although most of the aforementioned methods leads to significant improvements in coulombic efficiency, they are still far from enabling adequate performance in full cells. For this reason, many believe that lithium metal anodes will only be realized in conjunction with solid state electrolytes (SSEs). Efforts to do so are typically done by creating a dense SSE membrane to coat the surface of a lithium metal disc. Although this allows us to circumvent the issue of low coulombic efficiency of liquid electrolytes and safety concerns over using flammable liquids, migration of the SSE interface during cycling may lead to capacity fading. Additionally, many of the SSE materials of interest are unstable in contact with lithium metal, further hampering their performance. Thus far, interfacial engineering has only lead to modest improvements in cycling performance of lithium metal anodes.

### *Lithium Metal Hosts*

As previously mentioned, lithium dendrite formation arises from high local current densities. Under this consideration, many reports have utilized host materials with high surface area in order to reduce the local current density of lithium metal anodes. Porous carbons[40,69–72], polymers[73], and copper-based host materials such as copper nanosheets[74], submicron-thick copper skeletons grown on copper foils[75], and porous copper foams[76,77] have all been explored as potential host materials. Despite the broad body of work done on lithium metal hosts, most strategies require the use of complex fabrication processes, rendering them impractical for large-scale application.

### *Cell Design*

As stated earlier, the CE of a material must fall well above 99.9% in order to attain adequate cycling life. Bare Li metal may typically have CE values of around 90%, representing a dramatic barrier to overcome for practical full cells. In order to compensate for low coulombic efficiencies, lithium metal may be added in excess of the cathode in order to enable sufficiently long cycling life. However, this method effectively decreases the “useable” specific capacity of lithium depending on the amount of excess lithium added. Despite this, the extraordinarily high specific capacity of lithium and hostless nature still makes this a viable strategy for enabling lithium-ion batteries with high energy density.

## 6.4 Design and Process Overview

The cost and complexity of the aforementioned design strategies renders them impractical for commercial applications. The cost of lithium metal itself already greatly exceeds the cost of other materials for lithium-ion batteries. On top of this, the high reactivity of lithium metal necessitates the use of an inert atmosphere for cell fabrication, further increasing costs associated with lithium metal anodes. Although lithium metal suffers from a myriad of issues, cost and scalability requirements must always be considered for practical lithium metal anodes.

In order to overcome issues with cost and scalability faced by many of the previous reports on lithium metal hosts, we herein describe a design for porous Cu hosts for Li metal synthesized via a powder metallurgy strategy compatible for large-scale production. Additionally, we include the use of lithium metal passivation in order to enable cell assembly in ambient environment to circumvent the need for a high-cost dry room. A schematic for the synthesis process is depicted in Figure 6.3. Copper nitrate and sodium carbonate are combined in solution to form copper carbonate microparticles via precipitation. The resulting particles are filtered, dried, and annealed in a reducing environment to form porous Cu particles. The porous Cu particles are then compacted into a disk and dropped in molten Li to infiltrate Li into the disk, where the lithiated Cu disk is denoted Li-Cu. Finally, the disk is exposed to Freon R134a gas to form a passivating LiF layer on the surface of the disk to enable low-cost cell assembly. The resulting disk is denoted as Li-Cu-LiF.

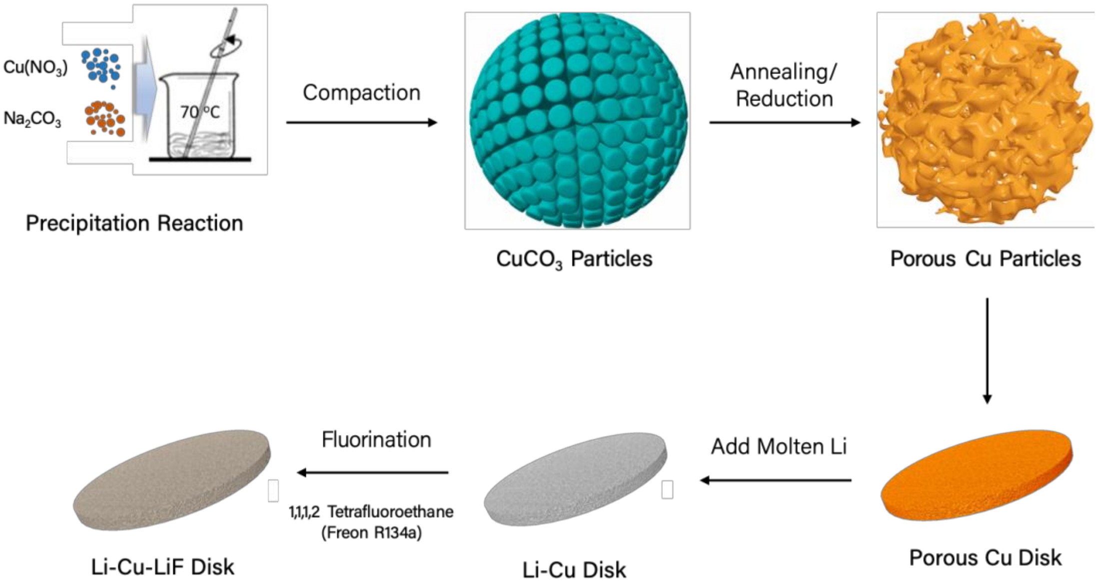

**Figure 6.3** Synthesis of prelithiated porous copper hosts with surface passivation.

## 6.5 Methods

*Synthesis of porous copper particles:* In a typical synthesis, a solution containing 7.23 g of $Cu(NO_3)_2\cdot 3H_2O$ in 100 mL $H_2O$ and a solution containing 3.18 g $Na_2CO_3\cdot 3H_2O$ in 100 mL $H_2O$ were prepared. Then, the $Na_2CO_3\cdot 3H_2O$ solution was slowly added into the $Cu(NO_3)_2\cdot 3H_2O$ solution under stirring and kept at room temperature for 10 min. The resulting solution was poured into a sealed glass bottle and kept at 70 $_{o}$C for 20 h without stirring. The resulting precipitates were collected via filtration, washed with $H_2O$, and finally dried at 70 $_{o}$C. The as-prepared precursor was annealed in a tube furnace under Ar/$H_2$ (the flow ratio of Ar and $H_2$ is 95:5) flow at 350 $_o$C for 3 h with a heating rate of 2 $_o$C min$_{-1}$ to obtain porous Cu particles.

*Fabrication of Li-Cu-LiF Electrodes:* 100 mg porous Cu particles were compacted into a disk using a mold with a 13 mm diameter and applying a weight of 1 T for 1.5 min. The Li melt-infusion was carried out in an Ar glove box containing less than 0.1 ppm oxygen and 0.1 ppm $H_2O$. Li foil (99.9%, MTI) was scraped and polished with a blade until shiny. Subsequently, Li foil was placed into a stainless-steel crucible and heated to 280 $_o$C on a hot plate and the porous Cu disk was placed on top of the molten Li, which steadily infiltrated into the porous Cu disk. To form the passivating LiF coating, the Li-Cu electrode was adhered to a stainless-steel disk with diameter of 15 mm, then placed into a sealed vessel with a clamp. Afterward, the vessel was vacuumed, charged to 100 KPa with Freon R134a gas and kept at 280 $_o$C for 20 h on a hot plate. Finally, the vessel was dissembled to obtain the Li-Cu-LiF electrode.

*Materials Characterizations:* XRD spectra were obtained with a Rigaku powder X-ray diffractometer (XRD) using Kα radiation ($\lambda = 1.54$ Å). Transmission electron microscopy (TEM) images were obtained with Titan S/TEM scanning transmission electron microscope (FEI). Scanning electron microscopy (SEM) images were taken with a Nova 230 Nano SEM. Raman spectra were obtained with a Renishaw 2000 System with a He/Ne laser at a wavelength of 633 nm. Gas sorption measurements were conducted using a Micromeritics ASAP 2020 system at 77 K. Prior to gas adsorption/desorption measurement, all power was degassed at 120 °C for 12 h. For X-ray photoelectron spectroscopy (XPS) studies, AXIS Ultra DLD was used for analysis. All the spectra were fitted to Gaussian–Lorentzian functions and a linear-type background using CasaXPS software. The binding energy values were all calibrated using C 1s peak at 284.5 eV.

*Electrochemical Characterizations:* All electrodes were assembled into 2032-type coin cells containing 1M lithium bis(trifluoromethanesulphonyl)imide (LiTFSI) dissolved in a mixture of 1,3-dioxolane (DOL)/1,2-dimethoxyethane (DME) (1:1 v/v) solution with 2 wt.% $LiNO_3$ additive as the electrolyte and porous polypropylene separators. Full cells were assembled using NCM111 as the cathode and 1M $LiPF_6$ in a mixture of ethyl carbonate and diethyl carbonate (1:1 v/v) as the electrolyte. To fabricate NCM111 electrodes, a slurry for the NCM111 powder consisting of carbon black and polyvinylidene fluoride (PVDF) at a weight ratio of 8:1:1 with N-methyl-2-pyrrilidone (NMP) as the solvent was casted on a piece of aluminum foil with a doctor blade. The slurry-coated aluminum foil was then dried at 90 $_{o}$C under vacuum overnight and cut into discs. The areal mass loading of cathode materials was 3 mg $cm_{-2}$. Electrochemical impedance spectroscopy (EIS) measurements were taken using an amplitude of 100 mV and frequencies ranging from 100 kHz to 10 mHz. Cycling performance was conducted with a LAND battery testing system (China). Specific capacities were calculated based on the total mass of the active material.

*Computational methods*: The projector augmented wave formalism of density functional theory (DFT) as implemented in the Cienna *Ab Initio* Simulation Package (VASP) was used for the system energy and electronic structure calculations. In order to get a better picture of weak interactions[78], we chose a computationally cost-effective “optB88-vdW” method for vdW interactions[79]. The exchange-correlation functional was approximated with the local density approximation[80]. The Gaussian smearing method[81] was used, and the width of smearing was chosen as 0.2 eV. The energy cutoff for plane-wave expansion of the PAW's was 400 eV. The supercell of the copper layer contains 48 Cu atoms. In the vertical direction, a vacuum layer of about 15 Å in thickness was introduced for all the surfaces and interfaces. The Brillouin zone[82] was sampled using Monkhorst-Pack scheme with a k-point mesh of 1×3×1 in the Gamma-centered grids for the structural relaxation, and 2×5×3 k-point mesh was used for the static calculations of all the systems. The structure relaxation was continued until the forces on all the atoms were converged to less than 0.01 eV/Å.

## 6.6 Results and Discussion

*Morphological Characterization*

Morphological characterizations of the Li-Cu-LiF disk at various stages during the fabrication process are displayed in Figure 6.4. After the precipitation reaction between copper nitrate and sodium carbonate, the resulting copper carbonate particles have a porous structure with size of around 4 μm (Figure 6.4a). After annealing in a reductive atmosphere, the resulting Cu particles retain its size but have altered pore morphology (Figure 6.4b). HRTEM imaging of the surface of the Cu particles (Figure 6.4c-d) reveal a lattice spacing of 0.216 nm, corresponding to the (111) plane of Cu, indicating the absence of surface oxidation. After compaction of the porous Cu particles (Figure 6.4e-f), the Cu particles endow the resulting disk with the same porous morphology as the individual particles. For this study, the disks prepared had a diameter of 1.3 cm$^2$ and a thickness of approximately 130 μm, although the thickness could be tuned by controlling the amount of Cu particles used. After infiltration of Li into the Cu disk, the resulting disk had a smooth surface with some Cu particles visible near the surface (Figure 6.4g-h). After reacting with Freon R134a to form a passivating LiF coating, the resulting Li-Cu-LiF disk (Figure 6.4i) retained the smooth surface seen in the Li-Cu disk. EDX mapping of the Li-Cu-LiF disk (Figure 6.4j-k) reveals uniform distribution of Cu and F moieties.

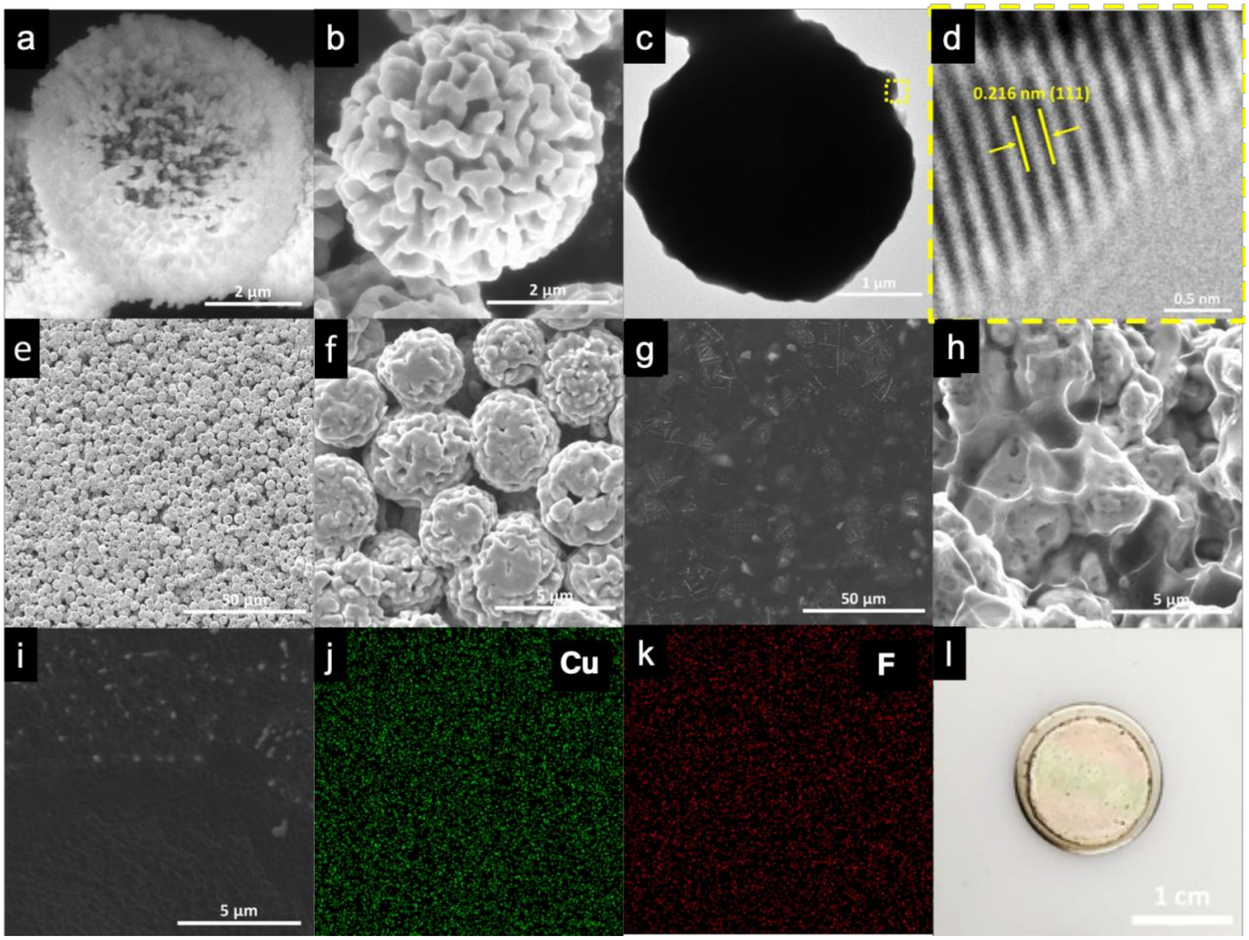

**Figure 6.4** Morphological characterization of Li-Cu-LiF at various stages of the fabrication process. a) SEM image of porous $Cu(CO_3)$ particles; b) SEM image of porous Cu particles; c) TEM image of porous Cu particle; d) High-resolution TEM image of the porous Cu particle shown in c); e-f) SEM of Cu disk; g-h) SEM of Li-Cu disk g) surface h) cross-section; i) SEM of Li-Cu-LiF disk; j-k) EDX mapping of the SEM image in i); l) Photograph of Li-Cu-LiF disk.

### *Structural and Chemical Characterization*

Structural and chemical characterizations of the various materials are presented in Figure 6.5. As seen in Figure 6.5a, the porous Cu disk displays excellent Li wettability in comparison to Cu foil. In order to explain this discrepancy, density functional theory (DFT) calculations were used to determine the interaction energy between Li and Cu. As shown in Figure 6.5b, a layer of copper atoms was constructed and an atom of lithium was placed above a copper atom, the center of two copper atoms, and the center of three copper atoms, resulting in Gibbs free energy changes of -2.46 eV, -2.37 eV, and -2.37 eV, respectively, confirming metallic copper is thermodynamically lithophilic. Based on the XPS results in Figure 6.5c revealing the presence of CuO on the Cu foil and not on the porous Cu disk, we can conclude that capillary force and the fresh, unoxidized surface of the porous Cu disk promotes the Li wettability and enables the infiltration of Li into the disk, as depicted in Figure 6.5d. XPS spectroscopy on the after reacting with Freon R134A with the Li-Cu disk (Figure 6.5e) reveals the presence of LiF. XRD spectroscopy on the copper carbonate and resulting Cu particles (Figure 6.5e-f) reveal that after annealing in a reductive atmosphere, the particles consist of pure Cu. The specific surface area of the Cu particles and porous Cu disk were 5.21 $m_2/g$ and 5.56 $m_2/g$, respectively, with the corresponding $N_2$ adsoprtion/desorption isotherms displayed in Figure 6.5g. As a reference the specific surface area of Cu foils are approximately 0.013 $m_2/g$, corresponding to over 400-fold increase in specific surface area for the Cu disk. The high specific surface area provides more sites for lithium metal deposition, which can reduce the local current density and inhibit the formation of lithium dendrites. The porous Cu disk attains an electrical resistivity of $1.12\times10_{-3}$ Ω/sq, which is comparable to that of Cu foil ($0.956\times10_{-3}$ Ω/sq), further suggesting the ability for the porous Cu disk to improve the performance of the electrode at elevated current densities.

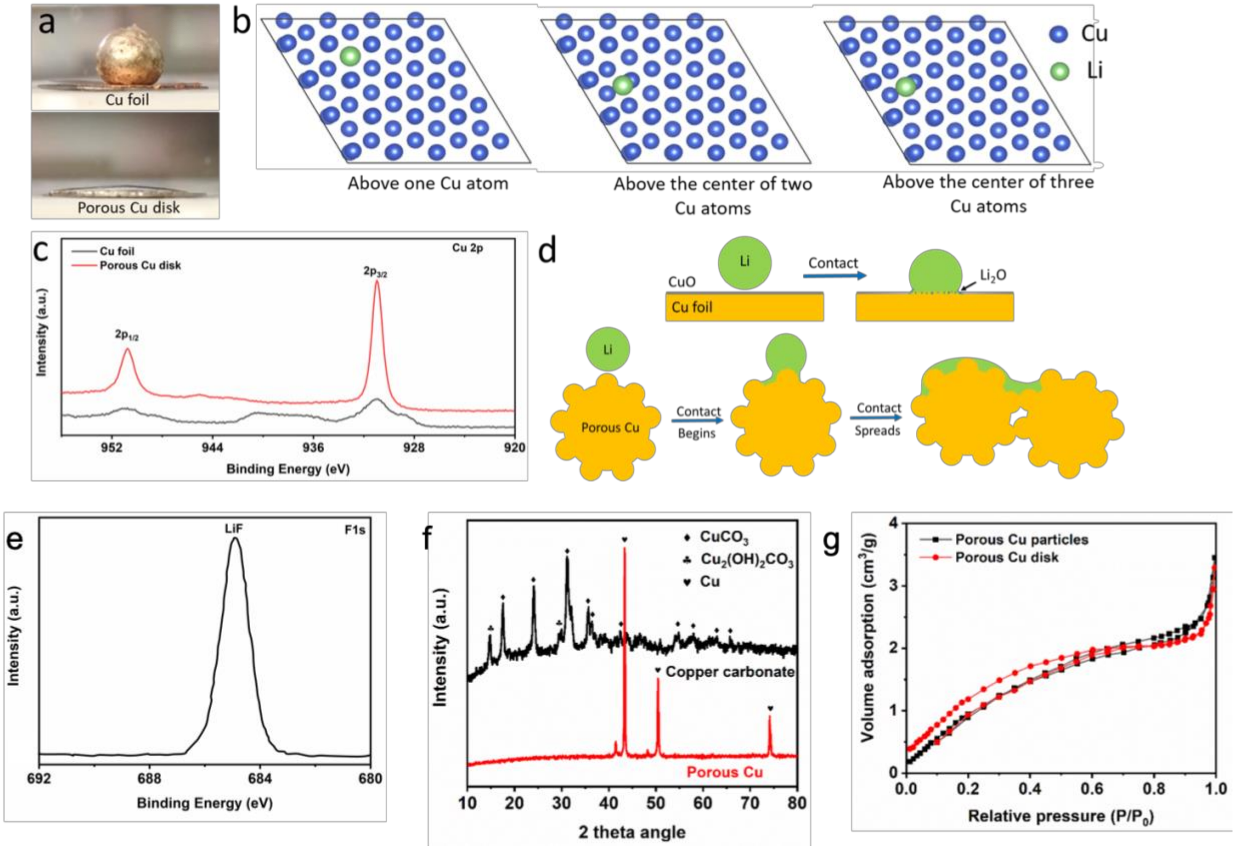

**Figure 6.5** Structural and chemical characterization of the Li-Cu-LiF disk at various stages of the fabrication process. a) Wetting of molten lithium on Cu foil and porous Cu disk; b) Top side views of a Li atom adsorbing above a Cu atom, above the center of two Cu atoms, and above the center of three Cu atoms after optimization; c) Cu 2p XPS spectra of Cu foil and porous Cu disk; d) A schematic illustration of the wetting process when a molten lithium droplet was placed on a Cu foil and a porous Cu disk; e) F 1s XPS spectrum of the Li-Cu-LiF disk; f) XRD spectra of the copper carbonate and porous Cu particles; g) $N_2$ adsorption/desorption isotherms of the porous Cu particles and porous Cu disk.

### *Electrochemical Characterization and Performance*

Symmetric cell electrochemical performance and corresponding morphologies for bare Li, Li-Cu, and Li-Cu-LiF are presented in Figure 6.6. Lithium plating and stripping were first examined using symmetric cells of LiF-Li-Cu, Li-Cu and bare Li at a current density of 1 mA/cm$_2$ and a total capacity of 1 mAh/cm$_2$ (Figure 6.6a). While bare Li exhibits rapidly increasing overpotential around 400 h, the Li-Cu and Li-Cu-LiF cells display minimal overpotential for 1,300 h and 1,600 h, respectively, suggesting the ability of the porous Cu disk to inhibit the growth of Li dendrites by virtue of a lower localized current density. Additionally, the prolonged stability of the Li-Cu-LiF disk compared to that of the Li-Cu disk suggests that the LiF coating also assists in prolongs the cycling life of the electrode by inhibiting side reactions between Li and the electrolyte. When cycled at current densities of 0.5, 1.0, 2.0 and 5.0 mA cm$_{-2}$ (Figure 6.6b), the Li-Cu-LiF displays smaller overpotential compared to Li-Cu and bare Li, further suggesting the ability of the ability of the LiF coating to enhance the cycling stability of the material. The corresponding EIS measurements (Figure 6.6c) indicate a smaller charge transfer resistance for Li-Cu-LiF and Li-Cu when compared to bare Li. The surfaces of the Li-Cu-LiF, Li-Cu, and bare Li electrodes were examined via SEM after 100 stripping/plating cycles at a current density of 1 mA/cm$_2$ and a capacity of 1 mAh/cm$_2$ (Figure 6.6d-f). While an abundance of Li dendrites can be seen in the bare Li electrode, the Li-Cu and Li-Cu-LiF electrodes show sheet-like Li deposition with the Li-Cu-LiF electrode having similar surface morphology to the pristine electrode. The air stability of was then assessed by exposing the electrodes to ambient air for 1 h before cell assembly. As seen in Figure 6.6g, the Li-Cu-LiF electrode displays minimal changes in appearance after 1 h, whereas the bare Li electrode was severely corroded, turning dark black. After exposure to ambient air for

1 h, symmetric cells were assembled for each electrode and cycled at a current density of 1 mA/cm$^2$ and a capacity of 1 mAh/cm$^2$ (Figure 6.6h). While the Li-Cu and bare Li cells show high overpotential, the Li-Cu-LiF cell displays remarkable cycling stability, demonstrating the effectiveness of the LiF coating to protect the Li metal from reacting with ambient air and ability to assemble full cells with existing infrastructure.

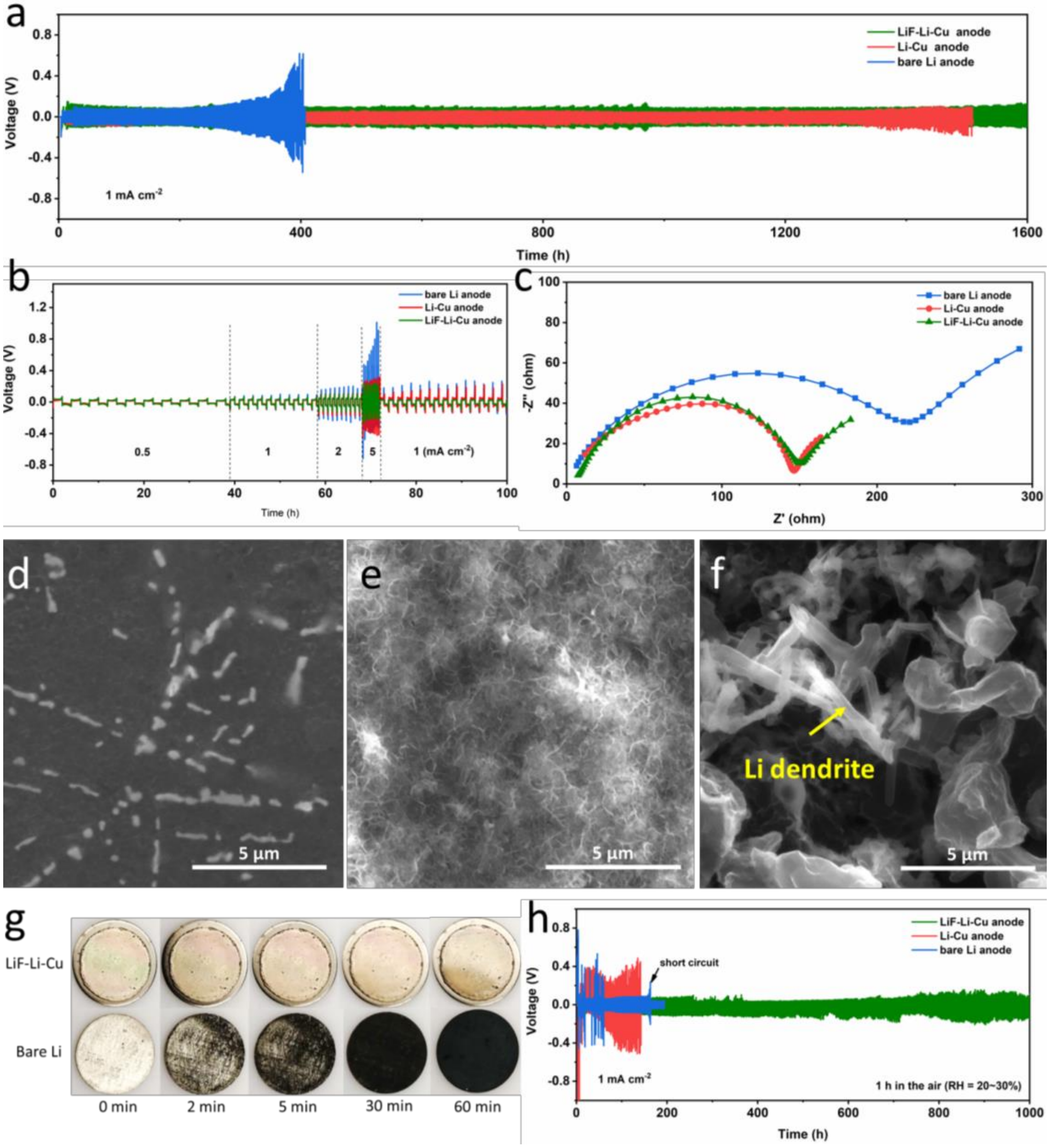

**Figure 6.6** Symmetric cell electrochemical performance and morphology of Li, Li-Cu, and Li-Cu-LiF after cycling. a) Galvanostatic cycling performance of the symmetric cells consisting of LiF-Li-Cu (green), Li-Cu (red) or bare Li (blue), which were operated at a current density of 1 mA/cm$_2$ and a plating/stripping capacity of 1 mAh/cm$_2$; b) The polarization vibration profiles at various current densities for symmetric cells consisting of LiF-Li-Cu, Li-Cu or bare Li. C) Nyquist plots of symmetric cells consisting of LiF-Li-Cu, Li-Cu or bare Li; SEM images of d) LiF-Li-Cu, e)

Li-Cu and f) bare Li after 100 repeated plating/stripping cycles at 1 mA/cm$_2$ with a capacity of 1 mAh/cm$_2$; g) Photographs of LiF-Li-Cu and bare Li anodes exposed to air with a RH of 20-30% for various times; h) Galvanostatic cycling performance of symmetric cells using LiF-Li-Cu (green), Li-Cu (red) or bare Li (blue) electrodes after exposure to ambient air for 1 h. The cells were operated at a current density of 1 mA/cm$_2$ with a plating/stripping capacity of 1 mAh/cm$_2$.

Full cells containing an NCM111 cathode were then assembled using Li-Cu-LiF, Li-Cu, and bare Li anodes (Figure 6.7). The rate performance for each cell (Figure 6.7a) was assessed at 0.2, 0.5, 1, 2 and 5 C (1 C = 170 mA/g). Both the cells with the Li-Cu-LiF and Li-Cu anodes deliver better rate performance than bare Li, confirming the advantage of using the porous Cu disk as a current collector. The Li-Cu-LiF cell shows a reversible capacity of 113 mAh g$_{-1}$ for 300 cycles at 0.5 C, corresponding to nearly 83% retention of the initial capacity. In contrast, cells with Li-Cu or bare Li show significantly lower capacity retentions of 47% and 27% after 300 cycles, respectively (Figure 6.7b). As seen in Figure 6.7c, the surface of the Li-Cu-LiF electrode displays no visual Li dendrites whereas few thick layers of Li dendrites are visible for the Li-Cu and bare Li electrodes, further suggesting the important role of the LiF coating in preventing Li dendrite growth.

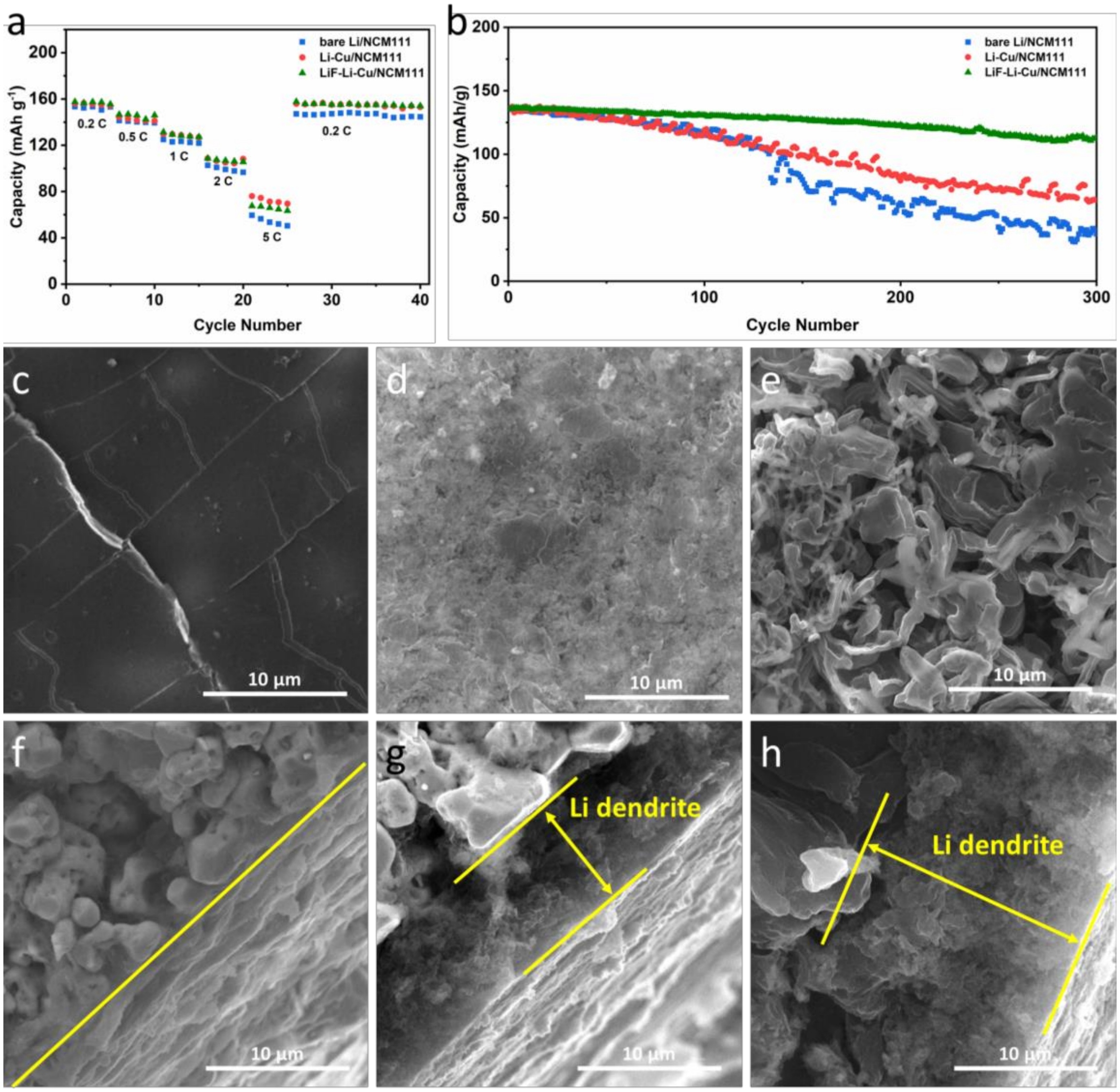

**Figure 6.7** Full cell electrochemical performance and corresponding morphological characterizations for cells paired with Li-Cu-LiF, Li-Cu, and bare Li anodes with NCM111 cathodes. a) rate performance of the full cells; b) cycling performance of the full cells at a rate of 0.5 C; SEM images of the surface of c) Li-Cu-LiF, d) Li-Cu, and e) bare Li electrodes and cross section of f) Li-Cu-LiF, g) Li-Cu, and h) bare Li electrodes after 100 cycles at 0.5 C in full cell configuration.

## 6.7 Conclusion and Significance

In this work, we present a design for porous Cu hosts for Li metal containing a LiF passivation layer with excellent cycling properties. Such a design allows for scalable production of Li metal anodes and cell assembly in existing infrastructure, which help overcome many of the aforementioned challenges with Li metal. The LiF passivation used is a robust method that can be applied to a wide range of lithium metal anode materials, providing a facile, low-cost method for improving performance and reducing cell fabrication costs.

## 6.8 Directions for Further Study

*Porous 3D N-Doped Graphene as Li Metal Hosts*

Previous reports have demonstrated that N-doped graphene is lithiophilic and reduces the nucleation overpotential required for Li metal deposition[40]. Considering that the design uses copper, a high-density material, substitution of Cu with N-doped graphene could theoretically improve the energy density of the material by virtue of decreasing the mass fraction of the electrochemically inactive current collector. This could theoretically be possible by using the existing porous Cu disk as a template for graphene growth, which allows the graphene to retain the porous structure of the Cu template and assist in the infiltration of Li metal and improvement in cycling performance compared to non-porous current collectors. However, the high mobility of Cu atoms at the temperatures required for CVD make this challenging since the aggregation of Cu particles during the process could destroy the porous structure. Despite this obstacle, the previously mentioned project on induction heating-mediated CVD may provide the means necessary to reduce aggregation of Cu particles to enable the construction of N-doped graphene with the porous Cu template.

### *Passivated Li-Si Alloys*

As stated earlier, one of the greatest challenges with developing silicon anode materials with adequate cycling performance is the large volumetric expansion of silicon during lithiation, leading to particle fracture, electrode pulverization, and repeated formation/fracture of the SEI, compromising cycling life. Previous reports have demonstrated that prelithiation of silicon is an effective means for producing anodes with improved cycling stability due to the fact that the electrode is fabricated in the fully expanded state, circumventing the need to provide additional void space[83,84]. However, such materials will likely need special atmospheres for cell assembly, much like Li metal anodes, which reduces the cost of cell fabrication. Using the same LiF coating technique as demonstrated in this work can likely provide a means to enable the preparation of electrode slurries containing prelithiated silicon and cell assembly in ambient environment, allowing one to access the improved cycling performance of lithiated silicon without the need to modify or increase the cost of the current electrode and cell assembly processes.

# References

1. P, P. *et al.* Coastal Systems and Low-Lying Areas. *Climate Change 2014: Impacts, Adaptation, and Vulnerability. Part A: Global and Sectoral Aspects. Contribution of Working Group II to the Fifth Assessment Report of the Intergovernmental Panel on Climate Change* (2014).
2. P, J. *et al.* Extreme storms. *Climate Science Special Report: Fourth National Climate Assessment, Volume I* (2017).
3. R, J. *et al.* Food Security and Food Production Systems. *Climate Change 2014: Impacts, Adaptation, and Vulnerability. Part A: Global and Sectoral Aspects. Contribution of Working Group II to the Fifth Assessment Report of the Intergovernmental Panel on Climate Change* (2014).
4. Ritchie, H. & Roser, M. $CO_2$ and Greenhouse Gas Emissions - Our World in Data. *Our World in Data* (2017).
5. Le Quéré. Global Carbon Project. *Carbon Dioxide Information Analysis Centre (CDIAC)* (2019).
6. Bereiter, B. *et al.* Revision of the EPICA Dome C CO2 record from 800 to 600 kyr before present. *Geophys. Res. Lett.* (2018).
7. Morice, C. P., Kennedy, J. J., Rayner, N. A. & Jones, P. D. Quantifying uncertainties in global and regional temperature change using an ensemble of observational estimates: The HadCRUT4 data set. *J. Geophys. Res.* **117,** n/a-n/a (2012).
8. Ellabban, O., Abu-Rub, H. & Blaabjerg, F. Renewable energy resources: Current status, future prospects and their enabling technology. *Renewable and Sustainable Energy Reviews*

**39,** 748–764 (2014).

9. Ritchie, H. & Roser, M. Energy - Our World in Data. *Our World in Data* (2014).
10. Hourly electricity consumption varies throughout the day and across seasons - Today in Energy - U.S. Energy Information Administration (EIA). at <https://www.eia.gov/todayinenergy/detail.php?id=42915>
11. Monthly Energy Review. *U.S. Energy Information Administration (EIA)* (2020).
12. 2017 Annual Merit Review, Vehicle Technologies Office (US Department of Energy, 2017).
13. Andre, D. *et al.* Future generations of cathode materials: an automotive industry perspective. *J. Mater. Chem. A* **3,** 6709–6732 (2015).
14. Schmuch, R., Wagner, R., Hörpel, G., Placke, T. & Winter, M. Performance and cost of materials for lithium-based rechargeable automotive batteries. *Nat. Energy* **3,** 267–278 (2018).
15. Portable Electronics Market Share 2019 Global Size, Industry Growth, Development Status, Opportunities, Segmentation, Competitive Landscape, Future Trends and Regional Forecast 2023 - MarketWatch. at <https://www.marketwatch.com/press-release/portable-electronics-market-share-2019-global-size-industry-growth-development-status-opportunities-segmentation-competitive-landscape-future-trends-and-regional-forecast-2023-2019-12-07>
16. Zubi, G., Dufo-López, R., Carvalho, M. & Pasaoglu, G. The lithium-ion battery: State of the art and future perspectives. *Renewable and Sustainable Energy Reviews* **89,** 292–308 (2018).
17. The Future of Drones in the Electric Power Industry. at <http://www.betaengineering.com/high-voltage-industry-blog/the-future-of-drones-in-the-

electric-power-industry>

18. FAA Approves AT&T Drones to Restore Cell Services in Puerto Rico - UAV Coach. at <https://uavcoach.com/drones-puerto-rico/>
19. Winter, M. & Brodd, R. J. What are batteries, fuel cells, and supercapacitors? *Chem. Rev.* **104,** 4245–4269 (2004).
20. Winter, M. & Besehard, J. *Handbook of Battery Materials*. 433–478 (Wiley VCH, 2011).
21. Nitta, N., Wu, F., Lee, J. T. & Yushin, G. Li-ion battery materials: present and future. *Materials Today* **18,** 252–264 (2015).
22. Pillot, C. The Rechargeable Battery Market and Main Trends 2016-2025. *Avicenne Energy* (2017).
23. Chen, J.-H., Jang, C., Xiao, S., Ishigami, M. & Fuhrer, M. S. Intrinsic and extrinsic performance limits of graphene devices on SiO2. *Nat. Nanotechnol.* **3,** 206–209 (2008).
24. Lee, J.-U., Yoon, D. & Cheong, H. Estimation of Young's modulus of graphene by Raman spectroscopy. *Nano Lett.* **12,** 4444–4448 (2012).
25. Sato, K., Noguchi, M., Demachi, A., Oki, N. & Endo, M. A mechanism of lithium storage in disordered carbons. *Science* **264,** 556–558 (1994).
26. Mabuchi, A. A survey on the carbon anode materials for rechargeable lithium batteries. *TANSO* **1994,** 298–306 (1994).
27. Ito, S., Murata, T., Hasegawa, M., Bito, Y. & Toyoguchi, Y. Study on CxN and CxS with disordered carbon structure as the anode materials for secondary lithium batteries. *J. Power Sources* **68,** 245–248 (1997).
28. Xue, J. S. Dramatic Effect of Oxidation on Lithium Insertion in Carbons Made from Epoxy Resins. *J. Electrochem. Soc.* **142,** 3668 (1995).

29. Winter, M., Besenhard, J. O., Spahr, M. E. & Novák, P. Insertion Electrode Materials for Rechargeable Lithium Batteries. *Adv. Mater. Weinheim* **10,** 725–763 (1998).

30. Bresser, D. & Passerini, S. handbook of battery materials . second edition; edited by claus daniel and jürgen o. besenhard. *Energy Technology* **1,** 617–618 (2013).

31. Juri, G., Wilhelm, H. A. & L'Heureux, J. High-purity graphite powders for high performance. *Ceramic Forum International* (2007).

32. Liang, G. & MacNeil, D. Lithium-Ion Batteries: Advanced Materials and Technologies Green Chemistry and Chemical Engineering. *CRC Press* (2011).

33. Dunn, J. B. *et al. Material and energy flows in the production of cathode and anode materials for lithium ion batteries*. (Argonne National Laboratory (ANL), 2015). doi:10.2172/1224963

34. Chehreh Chelgani, S., Rudolph, M., Kratzsch, R., Sandmann, D. & Gutzmer, J. A review of graphite beneficiation techniques. *Mineral Processing and Extractive Metallurgy Review* **37,** 58–68 (2016).

35. Hummers, W. S. & Offeman, R. E. Preparation of Graphitic Oxide. *J. Am. Chem. Soc.* **80,** 1339–1339 (1958).

36. Bhuyan, M. S. A., Uddin, M. N., Islam, M. M., Bipasha, F. A. & Hossain, S. S. Synthesis of graphene. *Int. Nano Lett.* **6,** 65–83 (2016).

37. Mo, R. *et al.* High-quality mesoporous graphene particles as high-energy and fast-charging anodes for lithium-ion batteries. *Nat. Commun.* **10,** 1474 (2019).

38. Li, Y. *et al.* Growth of conformal graphene cages on micrometre-sized silicon particles as stable battery anodes. *Nat. Energy* **1,** 15029 (2016).

39. Wu, H. *et al.* Stable Li-ion battery anodes by in-situ polymerization of conducting hydrogel

to conformally coat silicon nanoparticles. *Nat. Commun.* **4,** 1943 (2013).

40. Huang, G. *et al.* Lithiophilic 3D Nanoporous Nitrogen-Doped Graphene for Dendrite-Free and Ultrahigh-Rate Lithium-Metal Anodes. *Adv. Mater. Weinheim* **31,** e1805334 (2019).
41. Wang, H. *et al.* Wrinkled Graphene Cages as Hosts for High-Capacity Li Metal Anodes Shown by Cryogenic Electron Microscopy. *Nano Lett.* **19,** 1326–1335 (2019).
42. Chan, M. K. Y., Wolverton, C. & Greeley, J. P. First principles simulations of the electrochemical lithiation and delithiation of faceted crystalline silicon. *J. Am. Chem. Soc.* **134,** 14362–14374 (2012).
43. Liu, X. H. *et al.* Size-dependent fracture of silicon nanoparticles during lithiation. *ACS Nano* **6,** 1522–1531 (2012).
44. McDowell, M. T. *et al.* Studying the kinetics of crystalline silicon nanoparticle lithiation with in situ transmission electron microscopy. *Adv. Mater. Weinheim* **24,** 6034–6041 (2012).
45. Gauthier, M. *et al.* A low-cost and high performance ball-milled Si-based negative electrode for high-energy Li-ion batteries. *Energy Environ. Sci.* **6,** 2145 (2013).
46. Li, S. *et al.* High-rate aluminium yolk-shell nanoparticle anode for Li-ion battery with long cycle life and ultrahigh capacity. *Nat. Commun.* **6,** 7872 (2015).
47. Zhang, L. *et al.* A Yolk-Shell Structured Silicon Anode with Superior Conductivity and High Tap Density for Full Lithium-Ion Batteries. *Angew. Chem. Int. Ed. Engl.* **58,** 8824–8828 (2019).
48. Liu, N. *et al.* A yolk-shell design for stabilized and scalable li-ion battery alloy anodes. *Nano Lett.* **12,** 3315–3321 (2012).
49. Liu, N. *et al.* A pomegranate-inspired nanoscale design for large-volume-change lithium battery anodes. *Nat. Nanotechnol.* **9,** 187–192 (2014).

50. Veith, G. M. *et al.* Determination of the solid electrolyte interphase structure grown on a silicon electrode using a fluoroethylene carbonate additive. *Sci. Rep.* **7,** 6326 (2017).

51. Chen, T., Wu, J., Zhang, Q. & Su, X. Recent advancement of SiO x based anodes for lithium-ion batteries. *J. Power Sources* **363,** 126–144 (2017).

52. Jung, S. C., Kim, H.-J., Kim, J.-H. & Han, Y.-K. Atomic-Level Understanding toward a High-Capacity and High-Power Silicon Oxide (SiO) Material. *J. Phys. Chem. C* **120,** 886–892 (2016).

53. Blomgren, G. E. The development and future of lithium ion batteries. *J. Electrochem. Soc.* **164,** A5019–A5025 (2017).

54. Wiggers, H., Starke, R. & Roth, P. Silicon particle formation by pyrolysis of silane in a hot wall gasphase reactor. *Chem. Eng. Technol.* **24,** 261–264 (2001).

55. Doh, C.-H. *et al.* A new SiO/C anode composition for lithium-ion battery. *J. Power Sources* **179,** 367–370 (2008).

56. *Ball milling towards green synthesis: applications, projects, challenges*. (Royal Society of Chemistry, 2014). doi:10.1039/9781782621980

57. Wang, C. S., Wu, G. T. & Li, W. Z. Lithium insertion in ball-milled graphite. *J. Power Sources* **76,** 1–10 (1998).

58. Tikekar, M. D., Choudhury, S., Tu, Z. & Archer, L. A. Design principles for electrolytes and interfaces for stable lithium-metal batteries. *Nat. Energy* **1,** 16114 (2016).

59. Lin, D., Liu, Y. & Cui, Y. Reviving the lithium metal anode for high-energy batteries. *Nat. Nanotechnol.* **12,** 194–206 (2017).

60. Yan, K. *et al.* Selective deposition and stable encapsulation of lithium through heterogeneous seeded growth. *Nat. Energy* **1,** 16010 (2016).

61. Weitelman, U. Surface-passivated lithium metal and method for the production thereof, U.S. Patent 13,515,579. (2012).
62. Facadia, M. A 21st century lithium rush. *Industrial Minerals* (2017).
63. Global Lithium Report . *(Macquarie Research, 2016)*
64. Ding, F. *et al.* Dendrite-free lithium deposition via self-healing electrostatic shield mechanism. *J. Am. Chem. Soc.* **135,** 4450–4456 (2013).
65. Li, W. *et al.* The synergetic effect of lithium polysulfide and lithium nitrate to prevent lithium dendrite growth. *Nat. Commun.* **6,** 7436 (2015).
66. Stone, G. M. *et al.* Resolution of the Modulus versus Adhesion Dilemma in Solid Polymer Electrolytes for Rechargeable Lithium Metal Batteries. *J. Electrochem. Soc.* **159,** A222–A227 (2012).
67. Zheng, G. *et al.* Interconnected hollow carbon nanospheres for stable lithium metal anodes. *Nat. Nanotechnol.* **9,** 618–623 (2014).
68. Liu, F. *et al.* Fabrication of hybrid silicate coatings by a simple vapor deposition method for lithium metal anodes. *Adv. Energy Mater.* **8,** 1701744 (2017).
69. Xie, J. *et al.* Incorporating Flexibility into Stiffness: Self-Grown Carbon Nanotubes in Melamine Sponges Enable A Lithium-Metal-Anode Capacity of 15 mA h cm-2 Cyclable at 15 mA cm-2. *Adv. Mater. Weinheim* **31,** e1805654 (2019).
70. Zhang, Y. *et al.* High-capacity, low-tortuosity, and channel-guided lithium metal anode. *Proc. Natl. Acad. Sci. USA* **114,** 3584–3589 (2017).
71. Xue, P. *et al.* A Hierarchical Silver-Nanowire-Graphene Host Enabling Ultrahigh Rates and Superior Long-Term Cycling of Lithium-Metal Composite Anodes. *Adv. Mater. Weinheim* **30,** e1804165 (2018).

72. Song, R. *et al.* A 3D conductive scaffold with lithiophilic modification for stable lithium metal batteries. *J. Mater. Chem. A* **6,** 17967–17976 (2018).

73. Liu, Y. *et al.* Lithium-coated polymeric matrix as a minimum volume-change and dendrite-free lithium metal anode. *Nat. Commun.* **7,** 10992 (2016).

74. Huang, Z. *et al.* Realizing stable lithium deposition by in-situ grown Cu2S nanowires inside commercial Cu foam for lithium metal anodes. *J. Mater. Chem. A* (2018). doi:10.1039/C8TA10341K

75. Yang, C.-P., Yin, Y.-X., Zhang, S.-F., Li, N.-W. & Guo, Y.-G. Accommodating lithium into 3D current collectors with a submicron skeleton towards long-life lithium metal anodes. *Nat. Commun.* **6,** 8058 (2015).

76. Li, Q., Zhu, S. & Lu, Y. 3D Porous Cu Current Collector/Li-Metal Composite Anode for Stable Lithium-Metal Batteries. *Adv. Funct. Mater.* **27,** 1606422 (2017).

77. Qin, L. *et al.* Fabrication of Lithiophilic Copper Foam with Interfacial Modulation toward High-Rate Lithium Metal Anodes. *ACS Appl. Mater. Interfaces* **10,** 27764–27770 (2018).

78. Tkatchenko, A., DiStasio, R. A., Car, R. & Scheffler, M. Accurate and efficient method for many-body van der Waals interactions. *Phys. Rev. Lett.* **108,** 236402 (2012).

79. Hazrati, E., de Wijs, G. A. & Brocks, G. Li intercalation in graphite: A van der Waals density-functional study. *Phys. Rev. B* **90,** 155448 (2014).

80. Björkman, T., Gulans, A., Krasheninnikov, A. V. & Nieminen, R. M. Are we van der Waals ready? *J Phys Condens Matter* **24,** 424218 (2012).

81. Methfessel, M. & Paxton, A. T. High-precision sampling for Brillouin-zone integration in metals. *Phys. Rev. B* **40,** 3616–3621 (1989).

82. Froyen, S. Brillouin-zone integration by Fourier quadrature: Special points for superlattice

and supercell calculations. *Phys. Rev. B, Condens. Matter* **39,** 3168–3172 (1989).

83. Zhao, J. *et al.* Air-stable and freestanding lithium alloy/graphene foil as an alternative to lithium metal anodes. *Nat. Nanotechnol.* **12,** 993–999 (2017).
84. Zhao, J. *et al.* Metallurgically lithiated SiOx anode with high capacity and ambient air compatibility. *Proc. Natl. Acad. Sci. USA* **113,** 7408–7413 (2016).